Published in final edited form as:

Nature. 2017 February 23; 542(7642): 439–444. doi:10.1038/nature21394.

Inhibition decorrelates visual feature representations in the inner retina

Katrin Franke[1,2,3,4,*], **Philipp Berens**[1,2,3,*], **Timm Schubert**[1,3], **Matthias Bethge**[1,2,5,6], **Thomas Euler**[1,2,3,§], and **Tom Baden**[1,2,3,7,§]

[1] Centre for Integrative Neuroscience, University of Tübingen, Germany

[2] Bernstein Centre for Computational Neuroscience, Tübingen, Germany

[3] Institute for Ophthalmic Research, Tübingen, Germany

[4] Graduate School of Neural & Behavioural Sciences | International Max Planck Research School, University of Tübingen, Germany

[5] Institute for Theoretical Physics, University of Tübingen, Germany

[6] Max Planck Institute of Biological Cybernetics, Tübingen, Germany

[7] School of Life Sciences, University of Sussex, Brighton, UK

SUMMARY

The retina extracts visual features for transmission to the brain. Different types of bipolar cell split the photoreceptor input into parallel channels and provide the excitatory drive for downstream visual circuits. Anatomically and genetically, mouse bipolar cell types have been described at great detail, but a similarly deep understanding of their functional diversity is lacking. By imaging light-driven glutamate release from more than 13,000 bipolar cell axon terminals in the intact retina, we here show that bipolar cell functional diversity is generated by the interplay of dendritic excitatory inputs and axonal inhibitory inputs. The resultant centre and surround components of bipolar cell receptive fields interact to decorrelate bipolar cell output in the spatial and temporal domain. Our findings highlight the importance of inhibitory circuits in generating functionally diverse excitatory pathways and suggest that decorrelation of parallel visual pathways begins already at the second synapse of the mouse visual system.

§Correspondence at thomas.euler@cin.uni-tuebingen.de and tom@badenlab.org.
*Equal contributions
Correspondence and requests for materials should be addressed to T.E. (thomas.euler@cin.uni-tuebingen.de) and T.B. (tom@badenlab.org).

AUTHOR CONTRIBUTIONS

KF, PB, TE and TB designed the study; KF performed experiments and pre-processing; KF performed viral injections with help from TS; PB developed clustering with input from MB; KF, PB and TB analysed the data with input from TE; KF, PB, TE and TB wrote the manuscript.

Data (original data and clustering results) as well as Matlab code for visualisation are available from http://www.retinal-functomics.org.

The authors declare no competing financial interests. Readers are welcome to comment on the online version of the paper.

MAIN TEXT

The retina extracts visual features like motion or edges[1] and relays these to the brain through a diverse set of retinal ganglion cells (RGCs)[2,3]. This functional diversity starts to emerge already at the first retinal synapse, where in the mouse the visual signal is distributed from the photoreceptors onto 14 bipolar cell (BC) types (reviewed in ref.[4]). Their axon terminals stratify at different depths of the inner plexiform layer (IPL) and provide the excitatory drive for the feature extracting circuits of the inner retina.

Anatomically and genetically, the set of mouse BC types is well characterised[5–10]. Functionally, BCs have been classified mostly into broad categories like On and Off, transient and sustained or chromatic and achromatic[11–14]; however, a deeper understanding of their functional diversity and its origin is lacking.

Some of the observed functional differences between BC types are already established in the outer retina at the level of the BC dendrites[7,15–18]. In the inner retina, roughly 42 types of mostly inhibitory amacrine cell (AC) modulate BC output at the level of their synaptic terminals[5,19,20]. Although some AC circuits have been studied in depth (e.g. ref.[21,22]), we still understand only little about the general principles by which AC circuits help to decompose the visual scene into the parallel channels carried by the BCs.

Glutamate release units of the IPL

To address this important question, we used the glutamate biosensor iGluSnFR[23,24]. In contrast to presynaptic calcium changes, which have been used to assess BC function in mouse and zebrafish[25–28], glutamate release represents the output “currency” of BCs, not only accounting for presynaptic inhibition but also any release dynamics of BC ribbon synapses[29,30]. Using two-photon imaging we systematically characterised the glutamatergic output of mouse BCs at the level of individual axon terminals in the whole-mounted retina where long-range connections are preserved.

Intravitreal injection of AAV9.iGluSnFR yielded homogenous expression across the IPL (Fig. 1a), allowing for sampling of glutamate release at all IPL depths (Extended Data Fig. 1i). For each scan field, we registered the recording depth as its relative distance to the two plexi of SR101-stained blood vessels (Fig. 1b, Methods). To objectively define individual glutamate “release units”, we placed regions-of-interest (ROIs) in a single scan field (typically 48×12 μm at 32.125 Hz) using local image correlations (Fig. 1c, Extended Data Fig. 1, Supplementary Video. 1, Methods, Supplementary Discussion). We verified the ROI placement using calcium imaging of BCs with the GCaMP6f biosensor[31], where individual terminal systems and single axon terminals could be resolved (Extended Data Fig. 2).

We used a standardised set of four light stimuli (Fig. 1d, see also ref.[2]) to characterise BC output: (i) local (100 μm diameter) and (ii) full-field (600×800 μm) “chirp”-stimuli to probe response polarity as well as contrast and frequency preference of BC centre and centre-surround, respectively, (iii) 1 Hz full-field steps to study response kinetics and (iv) binary dense noise to estimate receptive fields (Methods). The light conditions on the retina corresponded to the low-photopic range (Methods).

ROIs in a single scan field showed typically two or more distinct response profiles (Fig. 1f), suggesting that multiple BC types could be recorded at a single IPL depth as expected from their stratification overlap[5,6,10] (cf. Fig. 2b). ROIs that shared a common response profile had RFs that either almost completely overlapped or were spatially offset (Fig. 1g), consistent with the reported tiling of BCs of the same type[8]. For example, the highly overlapping spatial RFs of the green ROIs suggest that they correspond to terminals not only of the same type of BC, but the same cell (Fig. 1g, Extended Data Fig. 2a–e). In contrast, the red ROIs likely correspond to terminals of two neighbouring cells of a second type (Fig. 1g). Therefore our ROIs likely reflect a reliable measure of BC output at the level of individual axon terminals.

Anatomy-guided functional clustering of mouse BCs

In total, we recorded light-evoked BC glutamate release from 13,311 ROIs (n=179 scan fields, n=37 mice) across the IPL. We assumed that (i) BCs are the main source of glutamate in the inner retina (Supplementary Discussion, Extended Data Fig. 3) and (ii) the catalogue of BCs in the mouse retina is complete with 14 types (5 Off-cone BCs (CBCs), 8 On-CBCs and the rod BC (RBC))[5,6,9,10], each tiling the retina[8]. Accordingly, the glutamate signals must map onto these 14 types of BCs including RBCs (Extended Data Fig. 2g–j, 4k–n). We took advantage of available EM-based BC axonal stratification profiles[6,10] to guide a functional clustering algorithm (Fig. 2a,b): For each scan taken at a specific IPL stratum, a prior probability for cluster allocation was computed from the relative axon terminal volume of all BC types in the respective IPL stratum (Fig. 2c, Extended Data Fig. 4a). We then extracted functional features from the glutamate responses that passed our quality criterion (76.9% of ROIs) using sparse PCA (Extended Data Fig. 4b) and clustered the ROIs using a modified Mixture of Gaussian model (Methods).

This yielded a functional fingerprint for every mouse BC type (Fig. 2d, Extended Data Fig. 4c). Most functional clusters were well-separated in feature space (Extended Data Fig. 4d–f); only few cluster pairs showed some overlap (e.g. C_{3a} and C_{3b} or C_{5t} and $C_{5o,}$ $d' \sim 2$). Because some BC types have highly overlapping stratification profiles, clusters $C_{1,2}$, $C_{3a,b,4}$, $C_{5a–c,X}$ and $C_{8,9,R}$ (Extended Data Fig. 4c) might need to be permuted. For simplicity, we refer to functional clusters by the anatomical BC profiles they originated from.

To validate our clustering approach, we visualised individual BC axon terminal systems by single-cell injection before glutamate imaging (Extended Data Fig. 5, Supplementary Discussion). At least 90% of all ROIs allocated to one terminal system were assigned to the same cluster or to functionally very similar clusters (Extended Data Fig. 5o.). This suggests that each of our functional clusters predominantly contains ROIs from a single BC type and therefore represents a valid approximation of its functional profile.

Organisational principles of the IPL

A fundamental principle of vertebrate inner retinal organisation is the subdivision into Off- and On-cells[13,32]. In agreement, $C_{1–4}$ increased activity at light-offset (Off-BCs), while $C_{5a\text{-}R}$ responded to light-onset (On-BCs, Fig. 2e). However, the segregation into On and Off

was not as clear-cut as expected: Off-BC clusters frequently responded with delayed spike-like events during the On phase of the light step (Extended Data Fig. 6a,g). These On events in Off-clusters did not correspond to spontaneous activity (Extended Data Fig. 6b). In contrast, On-BCs only rarely exhibited analogous Off responses (Extended Data Fig. 6b,g).

A second fundamental principle of inner retinal organisation is the segregation into temporal "transient" and "sustained" channels, which map onto the IPL centre and borders, respectively[11,24,28,33]. While our results are broadly in line with this notion, the full picture is more complex: For example, although spike-like events were observed most frequently towards the IPL centre (Extended Data Fig. 6d–g)[28], they could be found at all IPL depths. In addition, all On- but none of the Off-clusters showed a sustained plateau following an initial fast peak (Fig. 2f), implying different release dynamics in On- and Off-BCs. Interestingly, temporal BC properties like response delay ("fast" vs. "slow" onset), transience (speed of response decay) and the presence of spike-like events were not correlated (Extended Data Fig. 6i,j), suggesting that they can independently vary between BC types.

Finally, we found a spatial map across the IPL: RF size varied systematically among BC clusters and significantly decreased with increasing stratification depth (Fig. 2h, Extended Data Fig. 6h; mean: 66.3 and 55.9 μm for Off- and On-BC clusters, respectively). Despite this overall trend, RF sizes within one IPL depth differed substantially: For example, RF diameters of C_{3b} or C_{5a} were nearly 10 μm larger than those of C_4 or C_7, respectively.

In summary, our results highlight important exceptions from fundamental principles of inner retinal organisation and identify a new spatial organising principle. They indicate that functionally opposite signals such as short and long delays or even On versus Off response polarities co-exist at a single depth.

BC surround activation increases functional diversity

The abovementioned organising principles were extracted from the responses to the local chirp, yet responses to the full-field chirp were substantially more heterogeneous (Fig. 2d, Fig. 3). Additional surround stimulation significantly decorrelated chirp responses across clusters of the same polarity, and further anticorrelated responses of opposite polarity (Fig. 3a,b). This effect could be quite dramatic (Fig. 3c, Extended Data Fig. 6k): For example, On-clusters C_6 and C_9 responded nearly identical to the local chirp, whereas responses to the full-field chirp were decorrelated. This markedly broadened the response space covered by BC types (Extended Data Fig. 6l,m). For example, some On-BCs (e.g. C_{5a} or C_9) lost their sustained plateau phase during full-field stimulation and became much more transient (Fig. 2f vs. Extended Data Fig. 6m). Accordingly, the major type-specific differences in the final output of BCs appear to be determined by concomitant centre and surround activation, rather than centre activation alone.

Different ACs mediate and gate BC surround

We next dissected the cellular components underlying the observed surround effects using pharmacology. Two major groups of ACs modulate BC output at the level of the BC axon

terminal[34–36]: glycinergic small- and GABAergic wide-field ACs[37]. In addition, there is extensive cross-talk among ACs[38]. To test how these interactions modulate the BC surround, we pharmacologically blocked either GABA or glycine receptors while monitoring light-evoked glutamate release.

Pharmacological manipulation had little effect on overall response shape for local stimuli, but caused strong effects for full-field stimulation. Combined blocking of $GABA_A$ and $GABA_C$ receptors increased the response amplitude in both On- and Off-BCs (Extended Data Fig. 7a–c) and nearly eliminated the difference between local and full-field chirp responses (Fig. 4a–c, Extended Data Fig. 7d), consistent with attenuated surround inhibition[39–41]. This suggests that the BC surround is largely generated by presynaptic inhibition from GABAergic ACs (Supplementary Discussion).

In contrast, blocking glycine receptors reduced the response to full-field flashes (Extended Data Fig. 7a–c), consistent with an increase in surround strength due to disinhibition of the GABAergic network. This effect reliably induced a polarity switch in BC responses to full-field stimulation, anti-correlating local and full-field chirp responses (Fig. 4d–f, Extended Data Fig. 7e). Compared to this strong network effect of glycinergic ACs, direct glycinergic inputs to BCs e.g. via crossover inhibition acted more subtly on BC output, for example by decreasing tonic release of Off BCs (Extended Data Fig. 8, Supplementary Discussion)[42,43]. This suggests that in the whole-mounted retina, glycinergic ACs primarily modulate BC output in an indirect way by inhibiting GABAergic ACs, leading to decreased surround inhibition.

In summary, the two major groups of mouse ACs appear to act in tandem to set the ratio of excitation and inhibition in a group specific manner, thereby increasing functional diversity among BC types.

Differential centre-surround interactions underlie BC diversity

An increase in functional diversity upon surround stimulation is only possible if surround networks of different BC types differentially process visual stimuli. To obtain precise estimates of centre and surround spatio-temporal RFs, we estimated a series of linear time kernels at different distances from the BC RF centre by presenting a “ring noise” stimulus (Fig. 5a, Extended Data Fig. 9a).

Temporal properties of centre and surround time kernels were consistent across ROIs assigned to the same cluster, with pronounced differences between clusters (Extended Data Figs. 9b–d, 10a,d–g). Additionally, centre and surround time kernels of the same clusters were correlated with respect to width and time to peak (Extended Data Fig. 10d,e). Moreover, the spatial extent of surround kernels varied between types (Extended Data Fig. 10f, range: 255–410 μm), indicating that different AC networks are involved in different BC circuits.

We investigated how functional diversity may emerge from the differences in centre-surround properties. Using the spatial RFs, we first estimated the centre-surround ratio (CSR) for circular stimuli of different sizes (Fig. 5d, Extended Data Fig. 10h, Methods). For

an example cluster (C_X), a small stimulus (diameter: 100 μm) resulted in a two-fold stronger centre activation compared to the surround (CSR=2.3, "centre-dominant"). In contrast, the surround was stronger than the centre for a full-field spot (diameter: 500 μm, CSR=0.8, "surround-dominant"). All clusters gradually switched from a centre-dominant to a surround-dominant mode for diameters between 200 and 600 μm (Extended Data Fig. 10h).

We used a simple model to predict how the temporal properties of BCs change with stimulus diameter (Fig. 5e). For example, the predicted kernel of C_X doubled its centre frequency and temporal bandwidth with stimulus size (Fig. 5f). The model predicted cluster-specific changes in the temporal coding properties with increasing stimulus size, leading to an increase in the overall diversity across clusters (Fig. 5g), with kernels for larger stimuli encompassing a broader range of temporal frequencies. To test this prediction experimentally, we recorded BC kernels for two different stimulus diameters (100 and 500 μm). In agreement with the model, time kernels consistently differed between stimulus sizes (Fig. 5h), leading to lower time kernel correlations across clusters for centre-surround compared to centre- or surround-only stimulation (Fig. 5i, cf. Fig. 3a, Extended Data Fig. 10i,j). In addition, the model predicted that this effect is strongest between ~200 and 500 μm (Fig. 5j), matching the distribution of RF centre sizes of mouse RGCs[2].

Conclusions

Here, we systematically surveyed the functional diversity of mouse BCs by imaging their glutamatergic output. We showed how the temporal diversity is created by the interplay of the excitatory drive received at the dendrites and local axonal inputs from ACs. These two input streams combine at the BC axon terminal, the central computational unit of the IPL (discussed in ref.[4]). We showed that the streams are of comparable strengths but act at different spatial scales. Hence, the spatial structure of the visual input sets the ratio of excitation and inhibition and thus, the temporal encoding in BCs and consequently, the visual system. Possibly, there is even a finer level of computational granularity, as individual axon terminals of a single BC may signal independently, if they receive differential inputs from ACs (see Supplementary Discussion).

Why does the mouse retina split the visual signal into 14 parallel channels at the level of BCs? The finding that small stimuli in the range of a BCs dendritic field evoke highly correlated responses among types of the same response polarity implies that the set of BC types is not optimised to decompose the visual signal at this scale. Instead, it is only upon spatially extended stimulation that the rich functional diversity among BC types is revealed.

Our data suggests that this diversity is generated by the interaction of correlated yet not-identical pairs of temporal centre and surround RFs of BCs, with increasing stimulus size shifting the balance between centre- and surround-activation towards a stronger surround contribution. Here, different groups of ACs play distinct roles in setting up and gating the antagonistic surround (see Supplementary Discussion).

The notion that an antagonistic centre-surround RF organisation can decorrelate neural response properties is a fundamental principle in neuroscience (e.g. ref.[44,45]). For example,

surround-mediated decorrelation occurs in RGCs[46], as well as in visual cortex[47] and other sensory systems[48]. However, these studies focused on decorrelation between neurons independent of cell type. In contrast, less is known about the role of centre-surround RF organisation in decreasing the redundancy of the encoding between different neuronal cell types of the same class – as demonstrated here for the parallel signal channels formed by mouse BC types. Such decorrelation is typically linked to efficient coding[49] and our data place this computation already at the second synapse of the mouse visual system.

METHODS

Animals and tissue preparation

All animal procedures adhered to the laws governing animal experimentation issued by the German Government. For all experiments, we used 3- to 12-week-old B57Bl6 (n=3), Chat$^{tm2(cre)Lowl}$ (n=34; "ChAT:Cre", JAX 006410, The Jackson Laboratory, Bar Harbor, US), and Tg(Pcp2-cre)1Amc (n=5; "Pcp2", JAX 006207) mice of either sex. The transgenic lines were cross-bred with the Cre-dependent red fluorescence reporter line Gt(ROSA)26Sor$^{tm9(CAG-tdTomato)Hze}$ ("Ai9^{tdTomato}", JAX 007905) for a subset of experiments. Owing to the explanatory nature of our study, we did not use randomisation and blinding. No statistical methods were used to predetermine sample size.

Animals were housed under a standard 12 hr day/night rhythm. For recordings, animals were dark-adapted for ≥l h, then anesthetised with isoflurane (Baxter, Unterschleiβheim, Germany) and killed by cervical dislocation. The eyes were enucleated and hemisected in carboxygenated (95% O_2, 5% CO_2) artificial cerebral spinal fluid (ACSF) solution containing (in mM): 125 NaCl, 2.5 KCl, 2 $CaCl_2$, 1 $MgCl_2$, 1.25 NaH_2PO_4, 26 $NaHCO_3$, 20 glucose, and 0.5 L-glutamine (pH 7.4). Then, the tissue was moved to the recording chamber of the microscope, where it was continuously perfused with carboxygenated ACSF at ~37°C. The ACSF contained ~0.1 μM Sulforhodamine-101 (SR101, Invitrogen, Darmstadt, Germany) to reveal blood vessels and any damaged cells in the red fluorescence channel. All procedures were carried out under very dim red (>650 nm) light.

Virus injection

A volume of 1 μl of the viral construct (AAV9.hSyn.iGluSnFR.WPRE.SV40 or AAV9.CAG.Flex.iGluSnFR.WPRE.SV40 (referred to as "AAV9.iGluSnFR") or AAV9.Syn.Flex.GCaMP6f.WPRE.SV40, Penn Vector Core, Philadelphia, USA) was injected into the vitreous humour of 3- to 8-week-old mice anesthetised with 10% ketamine (bela-pharm GmbH & Co. KG, Vechta, Germany) and 2% xylazine (Rompun, Bayer Vital GmbH, Leverkusen, Germany) in 0.9% NaCl (Fresenius, Bad Homburg, Germany). For the injections, we used a micromanipulator (World Precision Instruments, Sarasota, USA) and a Hamilton injection system (syringe: 7634–01, needles: 207434, point style 3, length 51 mm, Hamilton Messtechnik GmbH, Hoechst, Germany). Due to the fixed angle of the injection needle (15°), the virus was applied to the ventro-nasal retina. Imaging experiments were performed 3 to 4 weeks after injection.

Single cell injection

Sharp electrodes were pulled on a P-1000 micropipette puller (Sutter Instruments, Hofheim, Germany) with resistances >100 mΩ. Single cells in the inner nuclear layer were dye-filled with 10 mM Alexa Fluor 555 (Life Technologies, Waltham, USA) in a 200 mM potassium gluconate (Sigma-Aldrich, Steinheim am Albuch, Germany) solution using the "buzz" function (50 ms pulse) of the MultiClamp 700B software (Molecular Devices, Biberach, Germany). Pipettes were carefully retracted as soon as the cell began to fill. Approximately 20 minutes were allowed for the dye to diffuse throughout the cell before imaging stated. After recording, an image stack was acquired to document the cell's morphology, which was then traced semi-automatically using the Simple Neurite Tracer plugin implemented in Fiji (http://Fiji.sc/Fihi).

Pharmacology

All drugs were bath applied for at least ten minutes before recordings. The following drug concentrations were used (in μM): 10 Gabazine (Tocris Bioscience, Bristol, UK)[50], 75 TPMPA (1,2,5,6-Tetrahydropyridin-4-yl)methylphosphinic acid, Tocris Bioscience)[50], 50 L-AP4 (L-(+)-2-Amino-4-phosphonobutyric acid, Tocris Bioscience) and 0.5 strychnine (Sigma-Aldrich)[51]. Drug solutions were carboxygenated and warmed to ~37°C before application. Pharmacological experiments were exclusively performed in the On and Off ChAT-immunoreactive bands, which are labelled in red fluorescence in ChAT:Cre c Ai9^{tdTomato} crossbred animals.

Two-photon imaging and light stimulation

We used a MOM-type two-photon microscope (designed by W. Denk, MPI, Heidelberg; purchased from Sutter Instruments/Science Products, Hofheim, Germany). Design and procedures were described previously[52]. In brief, the system was equipped with a mode-locked Ti:Sapphire laser (MaiTai-HP DeepSee, Newport Spectra-Physics, Darmstadt, Germany), two fluorescence detection channels for iGluSnFR or GCaMP6f (HQ 510/84, AHF/Chroma Tübingen, Germany) and SR101/tdTomato (HQ 630/60, AHF), and a water immersion objective (W Plan-Apochromat 20x/1,0 DIC M27, Zeiss, Oberkochen, Germany). The laser was tuned to 927 nm for imaging iGluSnFR, GCaMP6f or SR101, and to 1,000 nm for imaging tdTomato. For image acquisition, we used custom-made software (ScanM, by M. Müller, MPI, Martinsried, and T.E.) running under IGOR Pro 6.3 for Windows (Wavemetrics, Lake Oswego, OR, USA), taking time-lapsed 64 × 16 pixel image scans (at 31.25 Hz) for glutamate and 32 × 32 pixel image scans (at 15.625 Hz) for calcium imaging. For visualising morphology, 512 × 512 pixel images were acquired.

For light stimulation, we focused a DLP projector (K11, Acer) through the objective, fitted with band-pass-filtered light-emitting diodes (LEDs) ("green", 578 BP 10; and "blue", HC 405 BP 10, AHF/Croma) to match the spectral sensitivity of mouse M- and S-opsins. LEDs were synchronised with the microscope's scan retrace. Stimulator intensity (as photoisomerisation rate, 10^3 P*/s/cone) was calibrated as described previously[52] to range from 0.6 and 0.7 (black image) to 18.8 and 20.3 for M- and S-opsins, respectively. Due to technical limitations, intensity modulations were weakly rectified below 20% brightness. An additional, steady illumination component of ~10^4 P*/s/cone was present during the

recordings because of two-photon excitation of photopigments (for detailed discussion, see ref.[52] and ref.[53]). The light stimulus was centred prior to every experiment, such that its centre corresponded to the centre of the recording field. For all experiments, the tissue was kept at a constant mean stimulator intensity level for at least 15 s after the laser scanning started and before light stimuli were presented. Because the stimulus was projected though the objective lens, the stimulus projection plane shifted when focussing at different IPL levels. We therefore quantified the resulting blur of the stimulus at the level of photoreceptor outer segments. We found that a vertical shift of the imaging plane by 50 μm only slightly blurred the image (2% change in pixel width), indicating that different IPL levels (total IPL thickness = 41.6 ± 4.8 μm, mean ± s.d., n=20 scans) can be imaged without substantial change in stimulus quality.

Four types of light stimuli were used (Fig. 1): (*i*) Full-field (800×600 μm) and (*ii*) local (100 μm in diameter) "chirp" stimuli consisting of a bright step and two sinusoidal intensity modulations, one with increasing frequency (0.5–8 Hz) and one with increasing contrast, (*iii*) 1 Hz light flashes (500 μm in diameter, 50% duty cycle), and (*iv*) binary dense noise (20×15 matrix of 20×20 μm pixels; each pixel displayed an independent, balanced random sequence at 5 Hz for 5 minutes) for space-time receptive field (RF) mapping. In a subset of experiments, we used three additional stimuli: (*v*) A "ring noise" stimulus (10 annuli with increasing diameter, each annulus 25 μm wide), with each ring's intensity determined independently by a balanced 68 s random sequence at 60 Hz repeated four times, (*vi*) a surround chirp stimulus (annulus; Full-field chirp sparing the central 100 μm corresponding to the local chirp) and (*vii*) a spot noise stimulus (100 and 500 μm in diameter, respectively; intensity modulation like ring noise) flickering at 60 Hz. For all drug experiments, we showed in addition (*viii*) a stimulus consisting of alternating 2 s full-field and local light flashes (500 and 100 μm in diameter, respectively). All stimuli were achromatic, with matched photo-isomerisation rates for mouse M- and S-opsins.

Estimating recording depth in the IPL

For each scan field, we used the relative positions of the inner (ganglion cell layer) and outer (inner nuclear layer) blood vessel plexus to estimate IPL depth. To relate these blood vessel plexi to the ChAT bands, we performed separate experiments in ChAT:Cre × Ai9^{tdTomato} mice: High resolution stacks throughout the inner retina were recorded in the ventro-nasal retina. The stacks were then first corrected for warping of the IPL using custom-written scripts in IGOR Pro. In brief, a raster of markers (7 × 7) was projected in the x-y plane of the stack and for each marker the z positions of the On ChAT band were manually determined. The point raster was used to calculate a smoothed surface, which provided a z offset correction for each pixel beam in the stack. For each corrected stack, the z profiles of tdTomato and SR101 labelling were extracted by manually drawing ROIs in regions where only blood vessel plexi or the ChAT bands were visible. The two profiles were then matched such that 0 corresponded to the inner vessel peak and 1 corresponded to the outer vessel peak. We averaged the profiles of n=9 stacks from 3 mice and determined the IPL depth of On and Off ChAT band to be 0.48 ± 0.011 and 0.77 ± 0.014 (mean ± s.d.), respectively. The s.d. corresponds to an error of 0.45 and 0.63 μm for On and Off ChAT band, respectively. In the following, recording depths relative to blood vessel plexi were transformed into IPL

depths relative to ChAT bands for all scan fields (Fig. 1b), with 0 corresponding to the On ChAT band and 1 corresponding to the Off ChAT band.

Data analysis

Data analysis was performed using Matlab 2014b/2015a (The Mathworks Inc., Ismaning, Germany), and IGOR Pro. Data were organised in a custom written schema using the *DataJoint for Matlab* framework (github.com/datajoint/datajoint-matlab)[54]. All data as well as basic visualisation routines are available at www.retinal-functomics.org.

Pre-processing—Regions-of-interest (ROIs) were defined automatically by a custom correlation-based algorithm in IGOR Pro. For this, the activity stack in response to the dense noise stimulus (64 × 16 × 10,000 pixels) was first de-trended by high-pass filtering the trace of each individual pixel above ~0.1 Hz. For the 100 best responding pixels in each recording field (highest s.d. over time), the trace of each pixel was correlated with the trace of every other pixel in the field. Then, the correlation coefficient (ρ) was plotted against the distance of the two pixels and the average across ROIs was computed (Extended Data Fig. 1a). A scan field-specific correlation threshold ($\rho_{Threshold}$) was determined by fitting an exponential between the smallest distance and 5 µm (Extended Data Fig. 1b). $\rho_{Threshold}$ was defined as the correlation coefficient at x = λ, where λ is the exponential decay constant (space constant; Extended Data Fig. 1b). Next, we grouped neighbouring pixels with $\rho > \rho_{Threshold}$ into one ROI (Extended Data Fig. 1c–e). To match ROI sizes with the size of BC axon terminals, we restricted ROI diameters (estimated as effective diameter of area-equivalent circle) to range between 0.75 and 4 µm (Extended Data Fig. 1b,g). For validation, the number of ROIs covering single axon terminals was quantified manually for n=31 terminals from n=5 GCaMP6-expressing BCs (Extended Data Figs. 1g, 2a–c).

The glutamate (or calcium) traces for each ROI were extracted (as ΔF/F) using the image analysis toolbox SARFIA for IGOR Pro[55] and resampled at 500 Hz. A stimulus time marker embedded in the recorded data served to align the traces relative to the visual stimulus with 2 ms precision. For this, the timing for each ROI was corrected for sub-frame time-offsets related to the scanning. Stimulus-aligned traces for each ROI were imported into Matlab for further analysis.

For the chirp and step stimuli, we down-sampled to 64 Hz for further processing, subtracted the baseline (median of first 20–64 samples), computed the median activity $r(t)$ across stimulus repetitions (5 repetitions for chirp, >30 repetitions for step) and normalised it such that $\max_t(|r(t)|)=1$.

For dye-injected BCs, axon terminals were labelled manually using the image analysis toolbox SARFIA for IGOR Pro. Then, ROIs were estimated as described above and assigned to the reconstructed cell, if at least 2 pixels overlapped with the cell's axon terminals.

Receptive fields/Ring response kernel—We mapped the RF from the dense noise stimulus and the response kernel to the ring noise stimulus by computing the glutamate/calcium transient-triggered average. To this end, we used Matlab's findpeaks function to

detect the times t_i at which transients occurred. We set the minimum peak height to 1 s.d., where the s.d. was robustly estimated using:

$$\overline{\sigma}=\frac{median(|\dot{r}(t)|)}{0.6745}.$$

We then computed the glutamate/calcium transient-triggered average stimulus, weighting each sample by the steepness of the transient:

$$\boldsymbol{F}(x,y,\tau)=\frac{1}{M}\sum_{i=1}^{M}\dot{\boldsymbol{c}}(t_i)\boldsymbol{S}(x,y,t_i+\tau)$$

Here, $\boldsymbol{S}(x,y,t)$ is the stimulus, τ is the time lag and M is the number of glutamate/calcium events.

For the RF from the dense noise stimulus, we smoothed this raw RF estimate using a 3×3 pixel Gaussian window for each time lag separately and used singular value decomposition (SVD) to extract temporal and spatial RF kernels. To extract the RF's position and scale, we fitted it with a 2D Gaussian function using Matlab's lsqcurvefit. RF quality (Q_{iRF}) was measured as one minus the fraction of residual variance not explained by the Gaussian fit $\bar{F}_{map}$,

$$Qi_{\mathrm{RF}}=1-\frac{Var[F_{map}-\overline{F}_{map}]}{Var[F_{map}]}.$$

Other response measures

Response quality index: To measure how well a cell responded to a stimulus (local and full-field chirp, flashes), we computed the signal-to-noise ratio

$$Qi=\frac{Var[\langle \boldsymbol{C}\rangle_r]_t}{\langle Var[\boldsymbol{C}]_t\rangle_r},$$

where $\boldsymbol{C}$ is the T by R response matrix (time samples by stimulus repetitions) and $\langle\,\rangle x$ and $Var[]x$ denote the mean and variance across the indicated dimension, respectively[56].

For further analysis, we used only cells that responded well to the local chirp stimulus ($Qi_{Lchirp} > 0.3$) and resulted in good RFs ($Qi_{Lchirp} > 0.3$).

Polarity index: To distinguish between On and Off BCs, we calculated the Polarity index (POi) from the step response to local and full-field chirp, respectively, as

$$POi=\frac{\sum_{t=0}^{b} r(t+t_{stim\ on})-\sum_{t=0}^{b} r(t+t_{stim\ off})}{\sum_{t=0}^{b} r(t+t_{stim\ on})+\sum_{t=0}^{b} r(t+t_{stim\ off})},$$

where b = 2 s (62 samples). For cells responding solely during the On-phase of a step of light POi = 1, while for cells only responding during the step's Off-phase POi = −1.

Opposite polarity index: The number of opposite polarity events (*OPi*) was estimated from individual trials of local and full-field chirp step responses (first 6 seconds) using IGOR Pro's FindPeak function. Specifically, we counted the number of events that occurred during the first 2 seconds following the step onset and offset for Off and On BCs, respectively. For each trial the total number of events was divided by the number of stimulus trials. If OPi = 1, there was on average one opposite polarity event per trial.

High frequency index: The high frequency index (*HFi*) was used to quantify spiking (cf. ref.[57]) and was calculated from responses to individual trials of the local and full-field chirp, respectively. For the first 6 seconds of each trial, the frequency spectrum was calculated by fast Fourier transform (FFT) and spectra were averaged across trials for individual ROIs. Then, $HFi = \log(F_1/F_2)$, where F_1 and F_2 are the mean power between 0.5–1 Hz and 2–16 Hz, respectively.

Response transience index: The step response (first 6 seconds) of local and full-field chirps was used to calculate the response transience (*RTi*). Traces were up-sampled to 500 Hz and the response transience was calculated as

$$RTi=1-\frac{r(t_{max}+a)}{r(t_{max})},$$

where a = 400 ms is the read-out time following the peak response t_{max}. For a transient cell with complete decay back to baseline RTi =1, whereas for a sustained cell with no decay RTi =0.

Response plateau index: Local and full-field chirp responses were up-sampled to 500 Hz and the plateau index (*RPi*) was determined as:

$$RPi=1-\frac{r(t_{max}+a)}{r(t_{max})},$$

with the read-out time a = 2 s. A cell showing a sustained plateau has an RPi =1, while for a transient cell RPi =0.

Tonic release index: Local chirp frequency and contrast responses were up-sampled to 500 Hz and the baseline (response to 50% contrast step) was subtracted. Then, the glutamate

traces were separated into responses above (r_+) and below (r_-) baseline and the tonic release index (*TRi*) was determined as:

$$TRi = \frac{\sum_t |r_-(t)|}{\sum_t |r_+(t)| + |r_-(t)|}.$$

For a cell with no tonic release $TRi = 0$, whereas for a cell with maximal tonic release $TRi = 1$.

Response delay: The response delay (t_{delay}) was defined as the time from stimulus onset/offset until response onset and was calculated from the up-sampled local chirp step response. Response onset (t_{onset}) and delay (t_{delay}) were defined as

$$t_{onset} = \min[t | r(t) > 4\sigma_{baseline}],$$

and

$$t_{delay} = t_{onset} - t_{stim\ on/off}$$

respectively.

Feature extraction—We used sparse principal component analysis, as implemented in the SpaSM toolbox by K. Sjöstrang et al. (http://www2.imm.dtu.dk/projects/spasm/), to extract sparse response features from the mean responses across trials to the full-field (12 features) and local chirp (6 features), and the step stimulus (6 features) (as described in ref.[56], Extended Data Fig. 4b). Before clustering, we standardised each feature separately across the population of cells.

Anatomy-guided clustering—BC-terminal volume profiles were obtained from EM-reconstructions of the inner retina ref.[58,59]. To isolate synaptic terminals, we removed those parts of the volume profiles which likely correspond to axons. We estimated the median axon density for each type from the upper 0.06 units of IPL and subtracted twice that estimate from the profiles, clipping at zero. Profiles were smoothed with a Gaussian kernel (s.d.=0.14 units IPL depth) to account for jitter in depth measurements of two-photon data. For the GluMI cell, we assumed the average profile of CBC type 1 and 2.

We used a modified Mixture of Gaussian model[60] to incorporate the prior knowledge from the anatomical BC profiles. For each ROI i with IPL depth d_i, we define a prior over anatomical types c as

$$p_i(c) = \frac{IPL(d_i, c)}{\sum_k IPL(d_i, k)}$$

where $IPL(d,c)$ is the IPL terminal density profile as a function of depth and anatomical cell type. For example, all ROIs of a scan field taken at an IPL depth of 1.7 were likely to be sorted into clusters for CBC types 1 and 2, while a scan field taken at a depth of 0 received a bias for CBC types 5–7 (Extended Data Fig. 4a).

The parameters of the Mixture of Gaussian model are estimated as usual, with the exception of estimating the posterior over clusters. Here, the mixing coefficients are replaced by the prior over anatomical types, resulting in a modified update formula for the posterior:

$$\gamma_i(c)=\frac{p_i(c)N(x_i|\mu_c,\sum_c)}{\sum_{j=1\ldots K}p_i(j)N(x_i|\mu_j,\sum_j)}$$

All other updates remain the same as for the standard Mixture of Gaussians algorithm[61]. We constrained the covariance matrix for each component to be diagonal, resulting in 48 parameters per component (24 for the mean, 24 for the variances). We further regularised the covariance matrix by adding a constant (10^{-5}) to the diagonal.

The clustering was based on a subset (~83%) of the data (the first 11,101 recorded cells). The remaining ROIs were then automatically allocated to the established clustering (n=2,210 ROIs).

For each pair of clusters, we computed the direction in feature space that optimally separated the clusters

$$w=\sum^{-1}(m_1-m_2)$$

where m_i are the cluster means in feature space and Σ is the pooled covariance matrix. We projected all data on this axis and standardised the projected data according to cluster 1 (i.e. subtract the projected mean of cluster 1 and divide by its s.d.). We compute d' as a measure of the separation between the clusters:

$$d'=\overline{m_2}-\overline{m_1}$$

where $\overline{m_i}$ are the means of the two clusters in the projected, normalised space.

We also performed a more constrained clustering where we divided the IPL into 5 portions without overlap based on stratification profiles. We then clustered each zone independently using a standard Mixture of Gaussian approach and a cluster number determined by the number of BC types expected in each portion. The correlation between the cluster means of our clustering and the more constrained clustering was 0.97 for the full-field chirp traces, indicating high agreement.

Further statistical analysis

Field entropy: Field entropy (S_{Field}) was used as a measure of cluster heterogeneity within single recording fields and was defined as

$$S_{\mathrm{Field}} = -\sum_i p_i * log_2\, p_i,$$

where i is the number of clusters in one recording field and p_i corresponds to the number of ROIs assigned to the i^{th} cluster. $S_{Field} = 0$ if all ROIs of one recording field are assigned to one cluster and S_{Field} increases if ROIs are equally distributed across multiple clusters. In general, high field-entropy indicates high cluster heterogeneity within a single field.

Analysis of response diversity: To investigate the similarity of local and full-field chirp responses across clusters (Fig. 3), we determined the linear correlation coefficient between any two cluster pairs. The analysis was performed on cluster means. For every cluster, correlation coefficients were averaged across clusters with the same and opposite response polarity, respectively. We used principal component analysis (using Matlab's pca function) to obtain a 2D embedding of the mean cluster responses. The PCA was computed on all 14 local and 14 full-field cluster means. If not stated otherwise, the non-parametric Wilcoxon signed-rank test was used for statistical testing.

Pharmacology: To analyse drug-induced effects on BC clusters (Fig. 4, Extended Data Figs. 7,8), response traces and RFs of ROIs in one recording field belonging to the same cluster were averaged if there were at least 5 ROIs assigned to this cluster. Spatial RFs were aligned relative to the pixel with the highest s.d. before averaging.

Centre-surround properties: To estimate the signal-to-noise ratio of ring maps of single ROIs, we extracted temporal centre and surround kernels and normalised the respective kernel to the s.d. of its baseline (first 50 samples). For further analysis, we only included ROIs with $\mathrm{Peak}_{\mathrm{Centre}} > \pm 12$ s.d. and $\mathrm{Peak}_{\mathrm{Surround}} > \pm 7$ s.d., respectively. Ring maps of individual ROIs were then aligned relative to its peak centre activation and averaged across ROIs assigned to one cluster. For isolating BC surround, centre rings (first 2 rings) were cut and the surround time and space components were extracted by singular value decomposition (SVD). The surround space component was then extrapolated across the centre by fitting a Gaussian and an extrapolated surround map was generated. To isolate the BC centre, the estimated surround map was subtracted from the average map and centre time and space components were extracted by SVD. Estimated centre and surround maps were summed to obtain a complete description of the centre-surround structure of BC RFs. Across clusters, the estimated centre-surround maps captured 92.5 ± 1.9% of the variance of the original map. Due to low signal-to-noise ratio, temporal centre-surround properties of individual ROIs were extracted as described above using the centre and surround space kernels obtained from the respective cluster average.

The 1-dimensional gauss fits of centre and surround space activation were used to calculate centre and surround ratios (CSRs) for various stimulus sizes. Specifically, the CSR was defined as

$$CSR = \frac{\sum_{x=-S_r}^{x=S_r} Fit_{Centre}(x)dx}{\sum_{x=-S_r}^{x=S_r} Fit_{Surround}(x)dx},$$

where S_r corresponds to the stimulus radius and ranged from 10 to 500 μm, with a step size dx of 1 μm. Time kernels for different stimulus sizes were generated by linearly mixing centre and surround time kernels, weighted by the respective CSR.

BC spectra: Temporal spectra of BC clusters were calculated by Fourier transform of the time kernels estimated for a local (100 μm in diameter) and full-field (500 μm in diameter) light stimulus (see Centre-surround properties). Due to a lower S/N ratio of time kernels estimated for the full-field stimulus, kernels were cut 100 ms before and at the time point of response, respectively, still capturing 86.7 ± 14.7% of the variance of the original kernel. The centre of mass (*Centroid*) was used to characterise spectra of different stimulus sizes and was determined as

$$Centroid = \frac{\sum_{n=0}^{N-1} f(n)x(n)}{\sum_{n=0}^{N-1} x(n)},$$

where $x(n)$ corresponds to the magnitude and $f(n)$ represents the centre frequency of the n^{th} bin.

Surround chirp and spot noise data: To investigate the effect of surround-only activation and stimulus size on temporal encoding properties across BC clusters, response traces and estimated kernels of ROIs in one recording field belonging to the same cluster were averaged if there were at least 5 ROIs assigned to this cluster. Spectra for kernels estimated from local and full-field spot noise stimuli were calculated as described above.

Time kernel correlation: To analyse the similarity of temporal kernels estimated for a specific stimulus size (Fig. 5i,j), we computed the linear correlation coefficient of each kernel pair from clusters of the same response polarity. We then calculated the average correlation coefficient for every cluster (Fig. 5i) and further across all cluster averages (Fig. 5j).

Extended Data

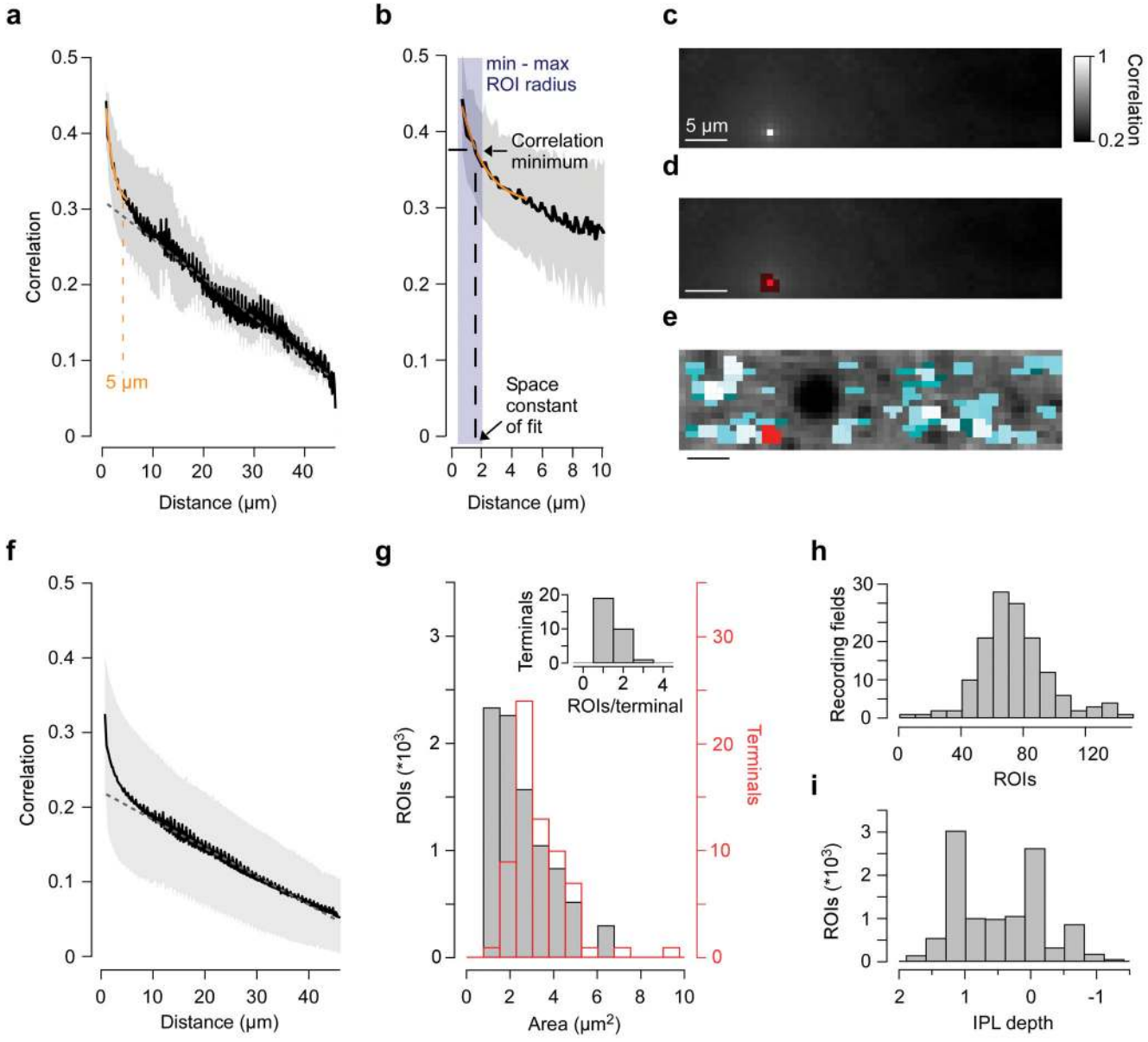

Extended Data Figure 1. ROI detection

a, Mean correlation (± s.d. shading, n=100 pixels) between noise-response traces of two individual pixels from scan field shown in (Fig. 1c) plotted against the distance of each pixel-pair (a_1). Dotted line shows linear fit to the data above x = 10 μm and its extrapolation towards x = 0 μm. The space constant obtained from an exponential fit (*orange*) for distances >5 μm was used to determine a scan field's specific correlation minimum for ROI detection (a_2, zoomed-in version of a_1). Blue shading indicates the range of allowed ROI radii (0.375–2 μm). **b,** Scan field from (Fig. 1c), with each pixel color-coded by its correlation with the noise trace of pixel indicated in (b_1). In b_2, the red shading corresponds to pixels with a correlation coefficient > correlation minimum from (a_2), resulting in red ROI in (b_3). **c,** As

(a_1), averaged for n=71 scan fields recorded at 48×12 µm. **d,** Histogram of ROI (*black*) and BC axon terminal (*red*) area. Terminal area was determined from BC axonal arborisations labelled in GCaMP6-injected Pcp2 mice where individual axon terminals can be distinguished (cf. SFig. 2a). Inset shows a histogram of the number of ROIs per BC axon terminal. **e,** Distribution of ROI numbers per scan field. **f,** Histogram illustrating sampling of ROIs against IPL depth. Data collected specifically for drug experiments (Methods) contributed to the "oversampling" of the two ChAT bands.

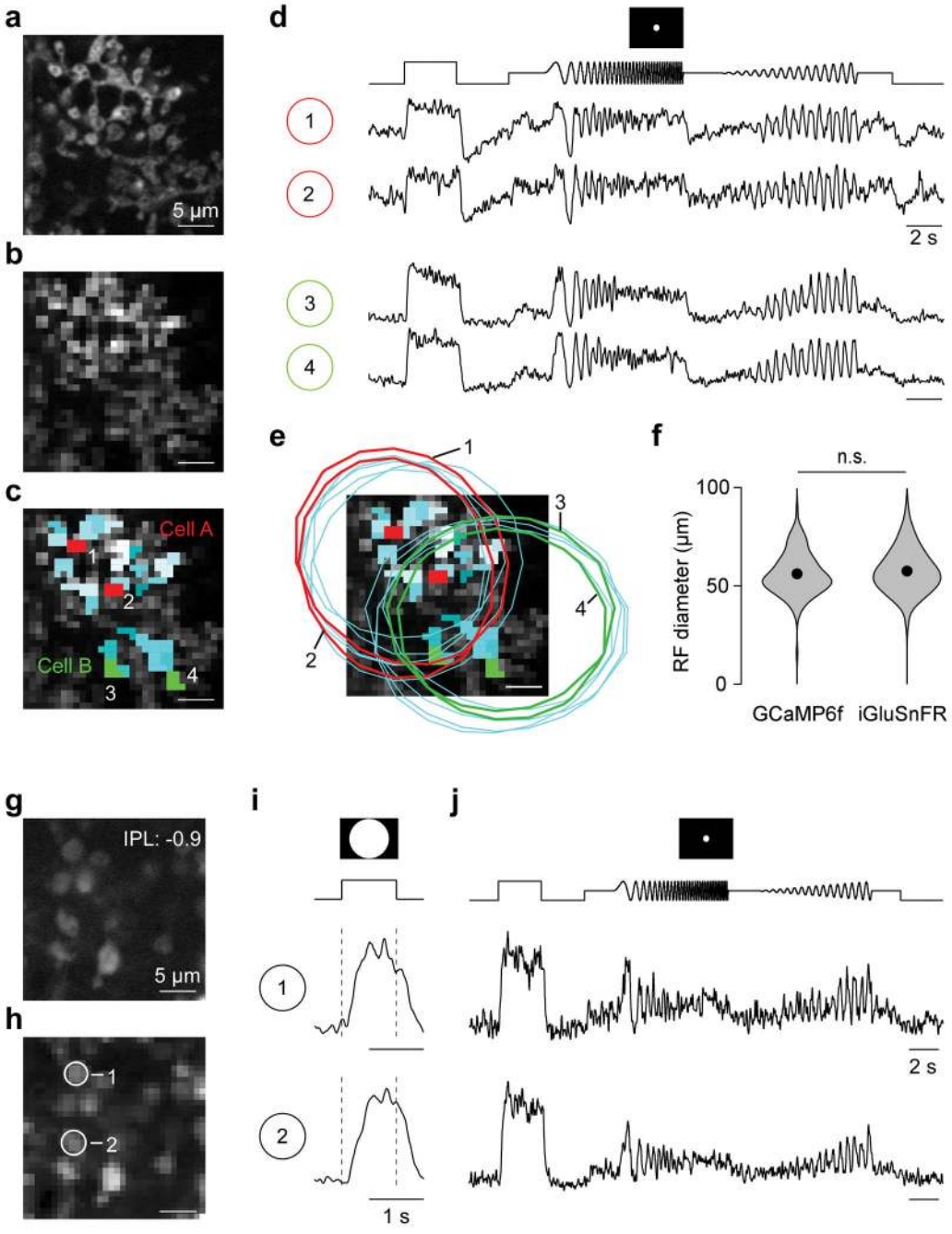

Extended Data Figure 2. GCaMP6 signals in mouse BC axon terminals

a–c, High resolution scan of GCaMP6f-expressing BC axon terminal systems in the IPL of a Pcp2 mouse (a) and corresponding scan field (b) with automatically generated ROI mask overlaid (c, cf. Extended Data Fig. 1). Our ROI algorithm reliably detected individual axon terminals and rather assigned two ROIs to a single terminal before merging two terminals into one ROI (cf. Extended Data Fig. 1g). **d,** Exemplary mean local-chirp responses of individual ROIs shown in (c) of the two different BCs shown in a. **e,** Scan field from (c) with ROI mask and spatial RFs (2 s.d. outlines of gauss fit) overlaid. **f,** Distribution of RF diameters estimated from On BC terminal calcium (GCaMP6) and glutamate release (iGluSnFR), respectively. Black dots correspond to mean RF diameters. Receptive field sizes estimated from calcium signals of single terminals closely fit those estimated from single iGluSnFR ROIs (56.1 ± 10 μm for GCaMP6 and 57.5 ± 10.6 μm for iGluSnFr; $p>0.05$, n=261 (GCaMP6) and n=3,540, non-parametric non-paired Wilcoxon signed-rank test) and matched the anatomical dimensions of BC dendritic fields (Wässle et al., 2009b; Behrens et al., 2016). The findings shown here suggest that each ROI likely captured the light-driven glutamate signal of at most one individual BC axon terminal. **g,h,** High resolution scan of GCaMP6-expressing RBC axon terminals (g) and corresponding scan field (h), with two individual terminals indicated. **i,j,** Mean responses of RBC terminals shown in (h) to full-field flashes (i, n=20 trials) and local chirp stimulus (j, n= 5 trials).

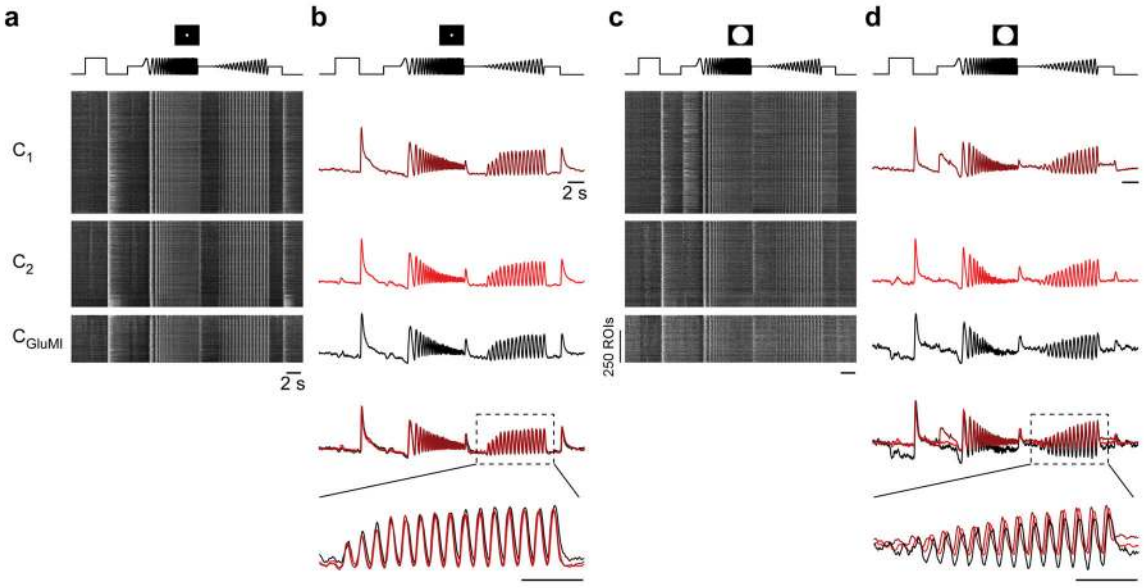

Extended Data Figure 3. Alternative clustering including the glutamatergic monopolar interneuron (GluMI)

a,b, Heat maps of local chirp responses of C_1, C_2 and C_{GluMI} (a) and respective cluster means (b). Superimposed cluster means (b, *bottom*) illustrate response similarity between clusters. **c** and **d** like a and b, but for full-field responses.

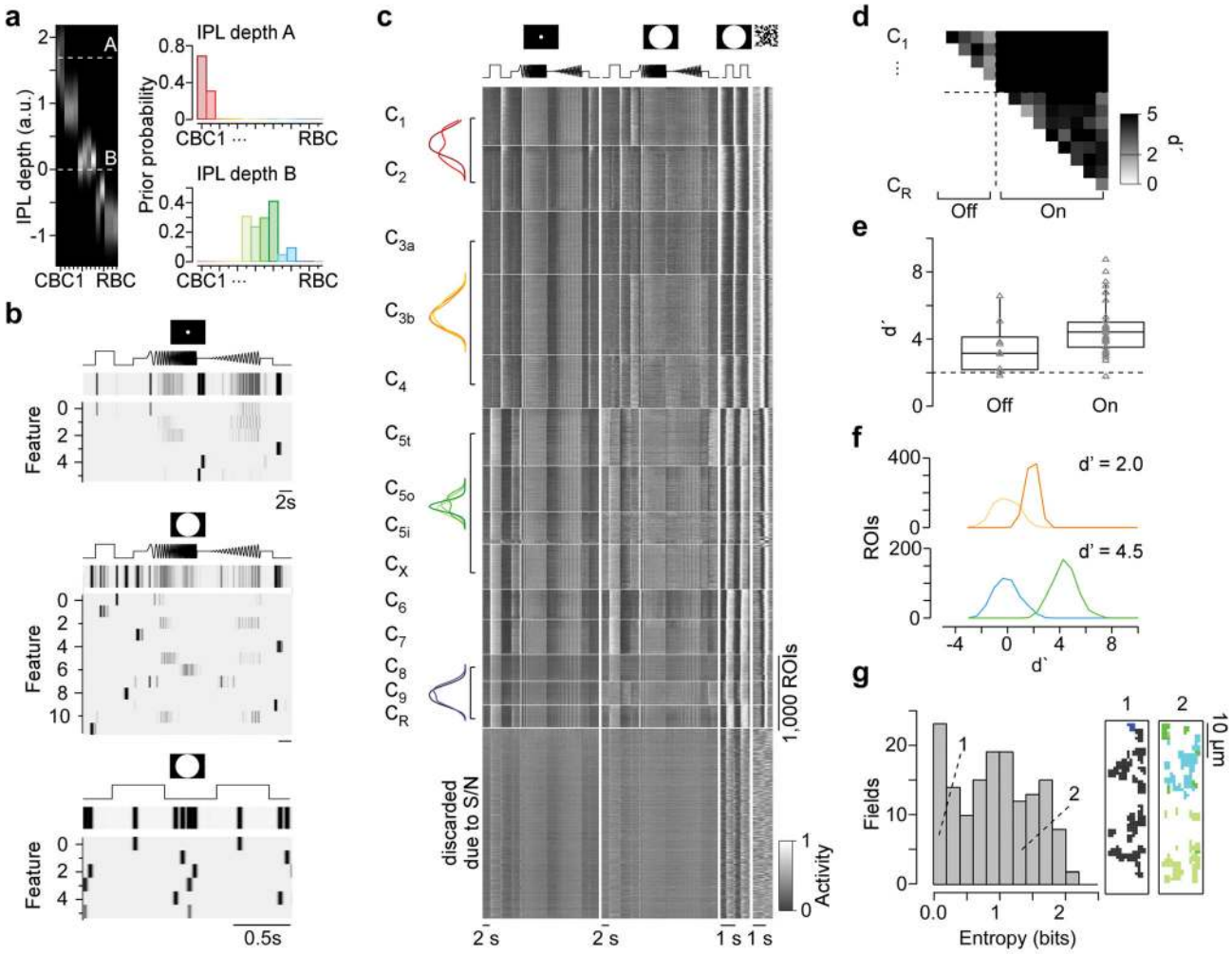

Extended Data Figure 4. Clustering

a, Exemplary distributions of prior probabilities for cluster allocation (*right*) taken from mean stratification profiles (*left*) of scan fields recorded at two different IPL depths (A: 1.7; B: 0). **b,** Temporal features extracted from glutamate traces in response to local (n=6 features, *top*) and full-field (n=12 features, *middle*) chirp and full-field flashes (n=6 features, *bottom*). **c,** Heat maps of all recorded glutamate responses (n=14 clusters plus ROIs discarded based on signal-to-noise (S/N) ratio) to the four visual stimuli (cf. Fig. 1); n=11,101 ROIs from 29 retinas. Each line corresponds to the responses of individual ROIs with activity colour-coded. Block height represents the number of included ROIs per cluster. Within one cluster, ROIs are sorted based on the quality of their RFs and local chirp response (Methods). Overlaid stratification profiles (*left*) illustrate overlap for some BC types. **d, e,** Cluster separation was determined for every cluster pair using the sensitivity index d′. Dotted lines in (d) illustrate transition between On and Off clusters and dotted line in e at d′=2, which corresponds to about 15% FP/FN rates. **f,** Separation of exemplary cluster pairs with a low (d′=2.0, *top*) and an average (d′=4.5, *bottom*) sensitivity index, respectively. **g,** Distribution of field entropies (*left,* Methods). Two exemplary scan fields

(*right*) with ROIs colour-coded by cluster allocation illustrate low (*1*) and high (*2*) field entropy, respectively.

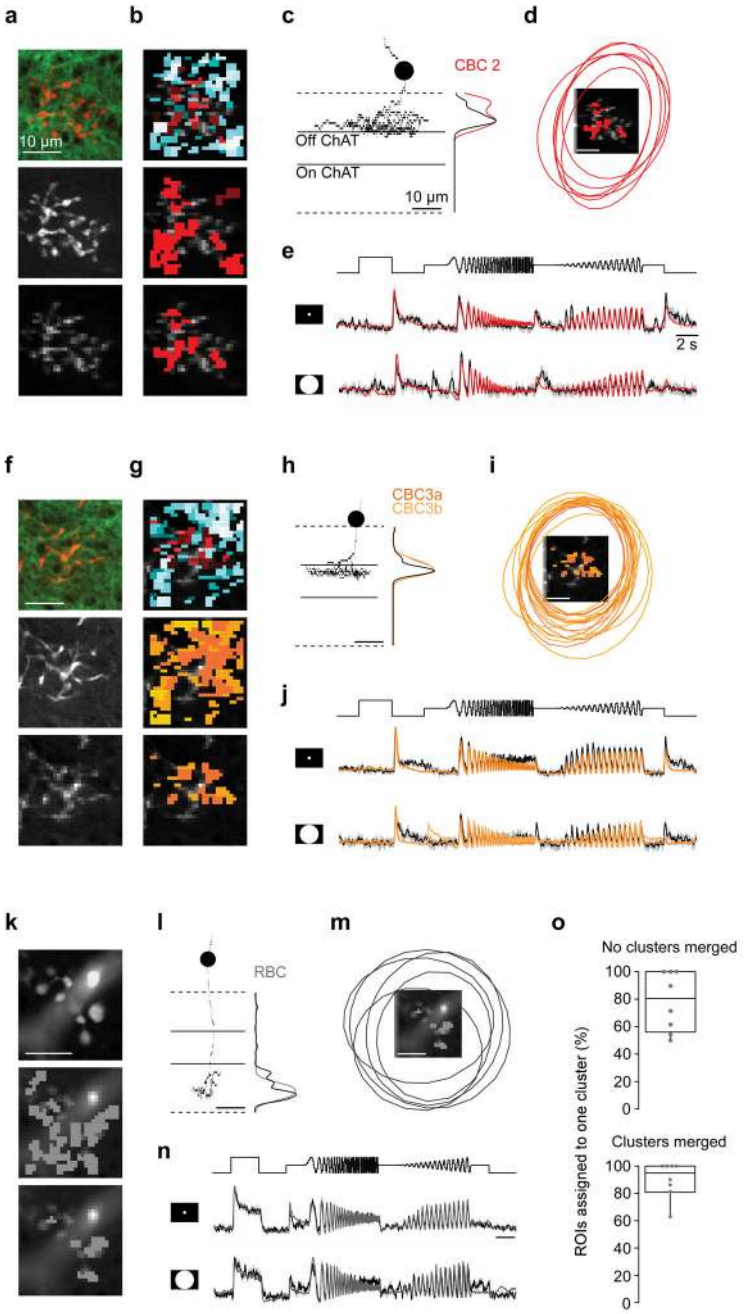

Extended Data Figure 5. Anatomical verification of clustering approach

a, High resolution scan of the axon terminal system of a filled BC (*middle*), with the iGluSnFR staining overlaid in green (*top*), and corresponding scan field (*bottom*). **b,** Colour-coded ROI mask (*cyan*), with ROIs assigned to the labelled axon terminal system in red (*top*; Methods). Cluster allocations of all ROIs, and ROIs assigned to the labelled cell that passed the quality criterion, are shown in the middle and bottom panel, respectively. **c,**

Reconstructed BC and its smoothed stratification profile (*black*), with the profile of the BC underlying the assigned functional cluster (CBC2) overlaid (*red*). **d,** RF outlines of ROIs with $Q_iRF < 0.6$ allocated to one reconstructed cell. **e,** Mean local (*top*) and full-field chirp (*bottom*) response of all ROIs assigned to the labelled cell (*black*), with s.d. shading (*grey*) and cluster mean of the assigned functional cluster (C_2, *red*). **f–j** like a–e and **k–n** like b–e. **o,** Box plots illustrate the fraction of ROIs from one cell that were assigned to the same cluster for all reconstructed BCs (n=8 cells, n=3 mice). For the plot in the bottom, functionally very similar clusters (C_{3a} and C_{3b}; C_{5o}, C_{5i} and C_{5t}) were merged. Due to lower signal-to-noise ratios and a slower sampling rate (15.625 Hz vs. 31.25 Hz) for this single-cell data compared to all other data, the fraction of "correctly" assigned ROIs is likely underestimated.

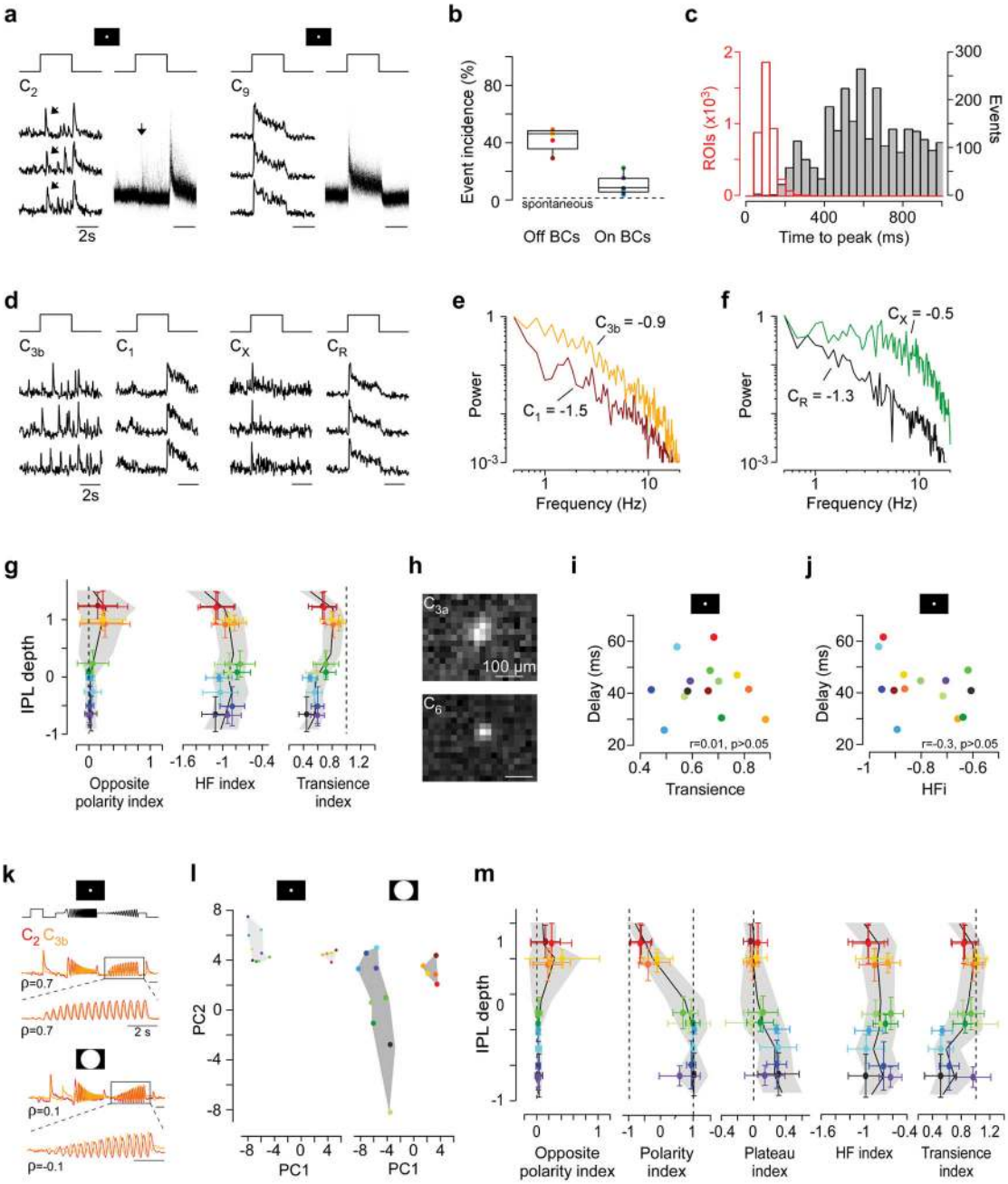

Extended Data Figure 6. Functional organisation of the IPL

a, Glutamate responses to the local chirp step stimulus (first 8 seconds) of single ROIs assigned to C_2 and C_9, respectively. Shown are responses to 3 trials and a histogram of response amplitudes across each cluster's 100 best responding ROIs. On responses in Off BC cluster C_2 are highlighted (*arrows*). **b,** Percentage of ROIs with at least one opposite polarity event in response to the local chirp step response for On and Off BC cluster. Dotted line illustrates mean incidence of spontaneous events (<1%). **c,** Time to peak of On events observed in the Off layer (*grey*) and On responses in On layer (*red*). Events were estimated from responses to single trials of the local chirp stimulus. Due to the variability in timing,

On events are not evident in traces averaged across the population of ROIs for each cluster (Fig. 2d). **d,** As (a), showing "spiking" (C_{3b}, C_X) and non-spiking (C_1, C_R) responses in clusters of either polarity. **e, f,** Mean spectra (n=5 trials) of local chirp step responses for two Off (C_{3b} and C_1) and two On (C_X and C_R) ROIs shown in (d), with HFi estimated from the relative power of low (0.5–1 Hz) and high (2–16 Hz) frequencies (Methods). **g,** Response measures estimated from local chirp responses for all ROIs plotted against IPL depth (cf. Fig. 2e–h). **h,** Spatial RFs of individual ROIs assigned to C_{3a} and C_6, respectively. **i,** Mean response transience of BC clusters is not correlated with mean response delay ($r=0.01$, $p>0.05$, $n=14$, linear correlation). **j,** Mean HFi and mean response delay are not correlated across BC clusters ($r=0.3$, $p>0.05$, $n=14$, linear correlation). **k,** Mean chirp responses of two Off (C_2 and C_{3b}) clusters, with linear correlation coefficient (ρ) of whole trace or contrast ramp indicated. **l,** Cluster means of local (*left*) and full-field (*right*) chirp responses embedded in two-dimensional feature space based on first and second principal components (PC). **m,** Response measures estimated from full-field chirp responses for all ROIs plotted against IPL depth (cf. Fig. 2e–h).

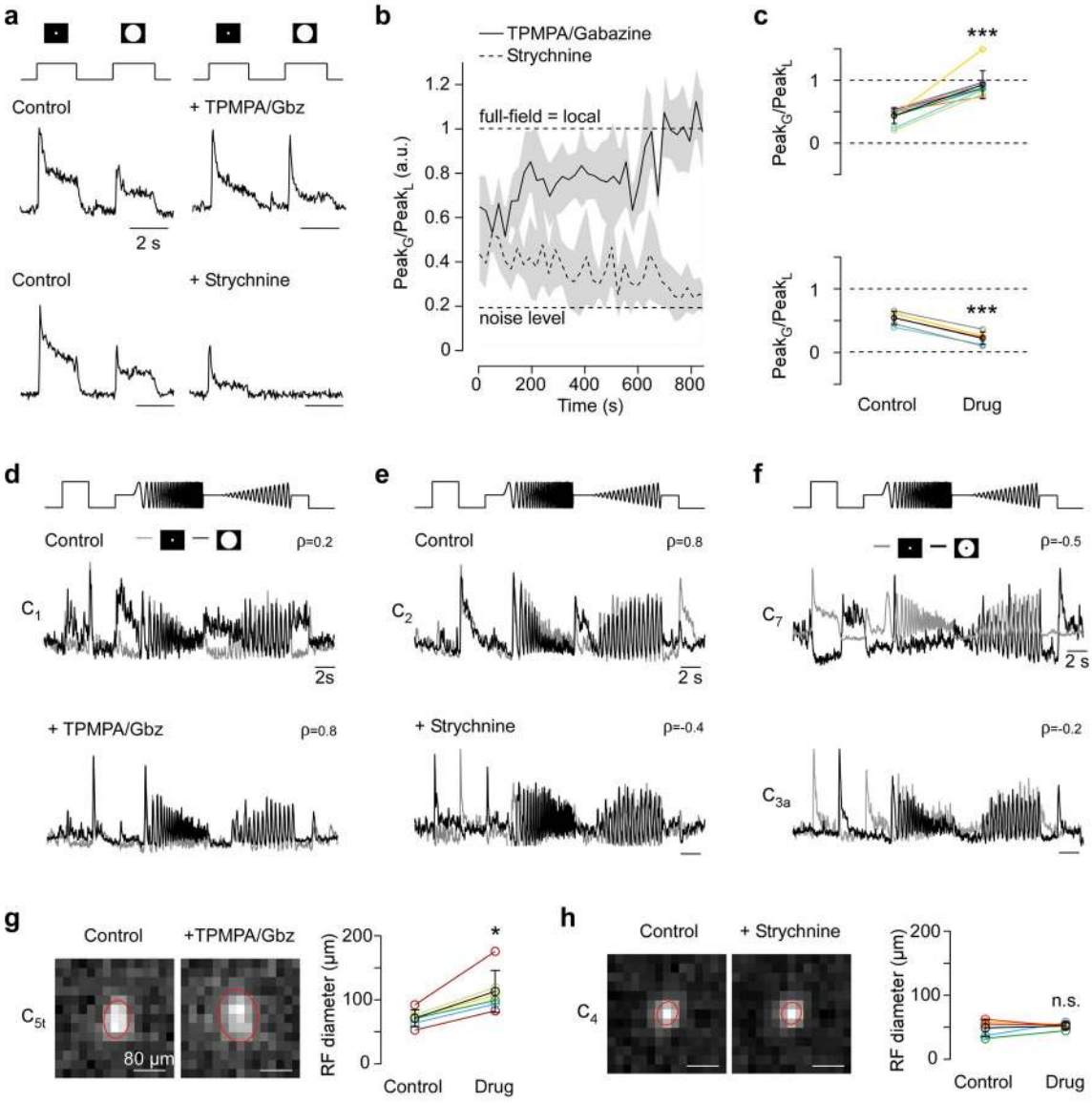

Extended Data Figure 7. GABA and glycinergic inhibition differentially shapes BC responses

a, Mean responses (n=5 trials) of individual ROIs to alternating local and full-field flashes under control conditions and with GABA (*top*) or glycine (*bottom*) receptor block. **b,** Change of mean peak amplitudes (± s.d. shading) of n=15 ROIs originating from two scan fields during wash-in of GABA and glycine receptor blockers, respectively. **c,** Drug-induced changes in peak response amplitude across different BC clusters upon blocking GABA (c_1; $p<0.001$, n=9 clusters from 5 scan fields and 4 mice, non-parametric paired Wilcoxon signed-rank test) and glycine receptors (c_2; $p<0.001$, n=6 clusters from 5 scan fields and 4 mice). Mean ± s.d. in black. **d,e,** Local (*grey*) and full-field (*black*) chirp responses for control and drug conditions (d: GABA receptor block; e: glycine receptor block), with linear correlation coefficient (ρ) between each pair indicated. **f,** Local (*grey*) and surround (*black*) chirp responses for an exemplary On (C_7, *top*) and Off (C_{3a}, *bottom*) BC cluster, respectively. **g,h,** Spatial RFs with 2 s.d. outline of Gaussian fit shown in red (*left*) and

quantification of changes in RF diameter across different BC clusters (*right*) upon blocking GABA (g; $p<0.05$, n=6 cluster from 3 scan fields and 2 mice, non-parametric paired Wilcoxon signed-rank test) and glycine receptors (h; $p>0.05$, n=5 cluster from 3 scan fields and 2 mice).

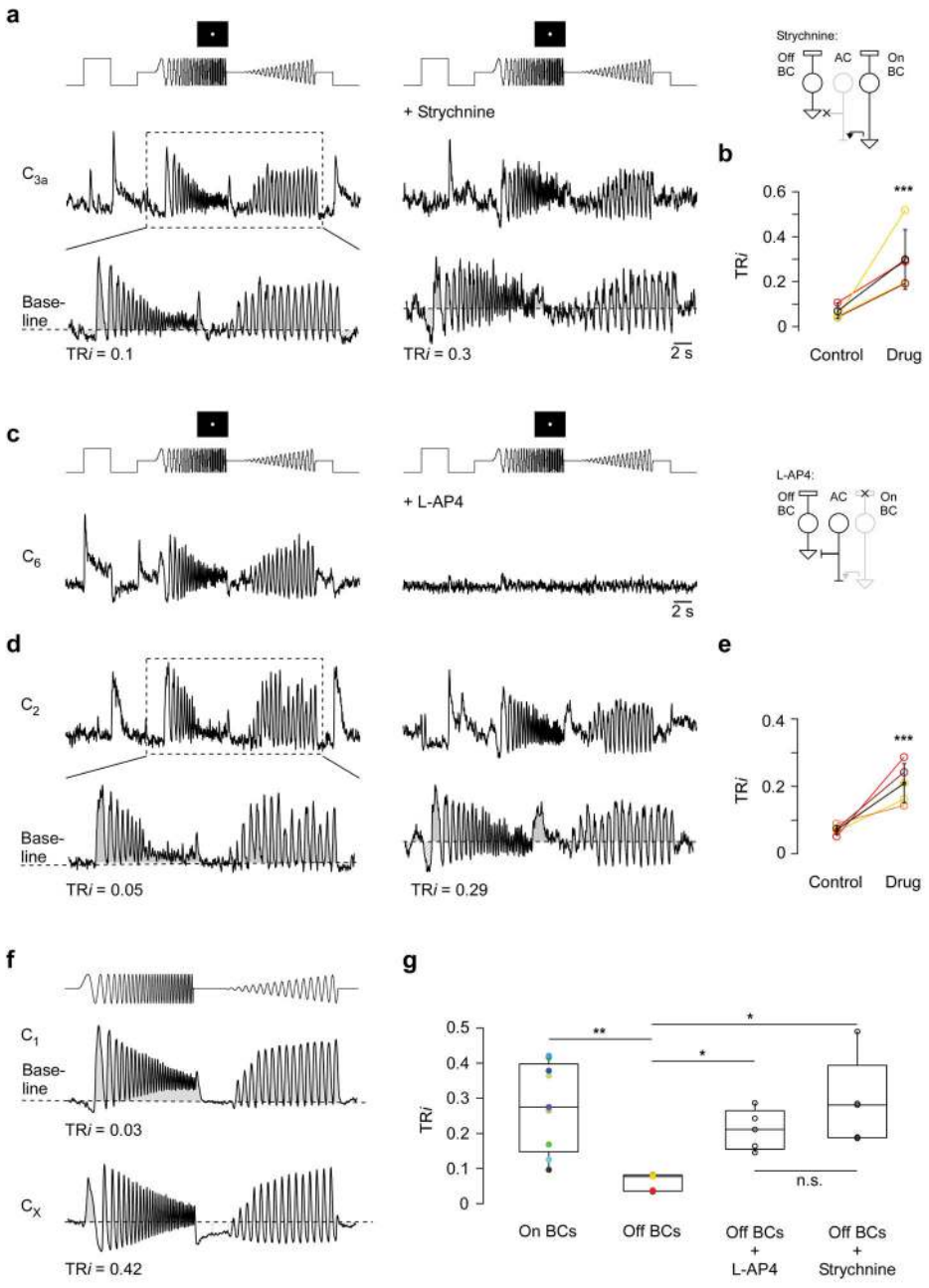

Extended Data Figure 8. Glycine-mediated crossover inhibition from the On pathway rectifies Off BCs

a, Local chirp traces of an exemplary Off BC cluster (C_{3a}) during control condition (*left*) and glycine receptor block (*right*). Magnified traces in the bottom illustrate an increase in tonic release upon drug application, with respective tonic release indices (TR*i*, Methods)

indicated. Dotted line corresponds to baseline. Schematic (*top right*) illustrates effect of drug on inner retinal network. **b,** Quantification of drug-induced changes in tonic release across different Off BC clusters ($p<0.001$, n=5 clusters from 5 scan fields and 4 mice, non-parametric paired Wilcoxon signed-rank test). **c,** Local chirp responses of an exemplary On (C_6) and Off (**d**, C_2) BC cluster for control condition (*left*) and upon blocking the On BC pathway via L-AP4 (*right*). **e,** Tonic release indices of different Off BC clusters for control and L-AP4 condition ($p<0.001$, n=5 clusters from 3 scan fields and 2 mice, non-parametric paired Wilcoxon signed-rank test). **f,** Average local chirp frequency and contrast responses of an exemplary Off (C_1, *top*) and On (C_X, *bottom*) BC cluster illustrate rectification of Off BC responses. **g,** Comparison of tonic release indices of On and Off BC clusters under control condition and Off BCs upon blocking crossover inhibition with L-AP4 or strychnine (*$p<0.05$, **$p<0.01$, non-parametric Kruskal-Wallis test).

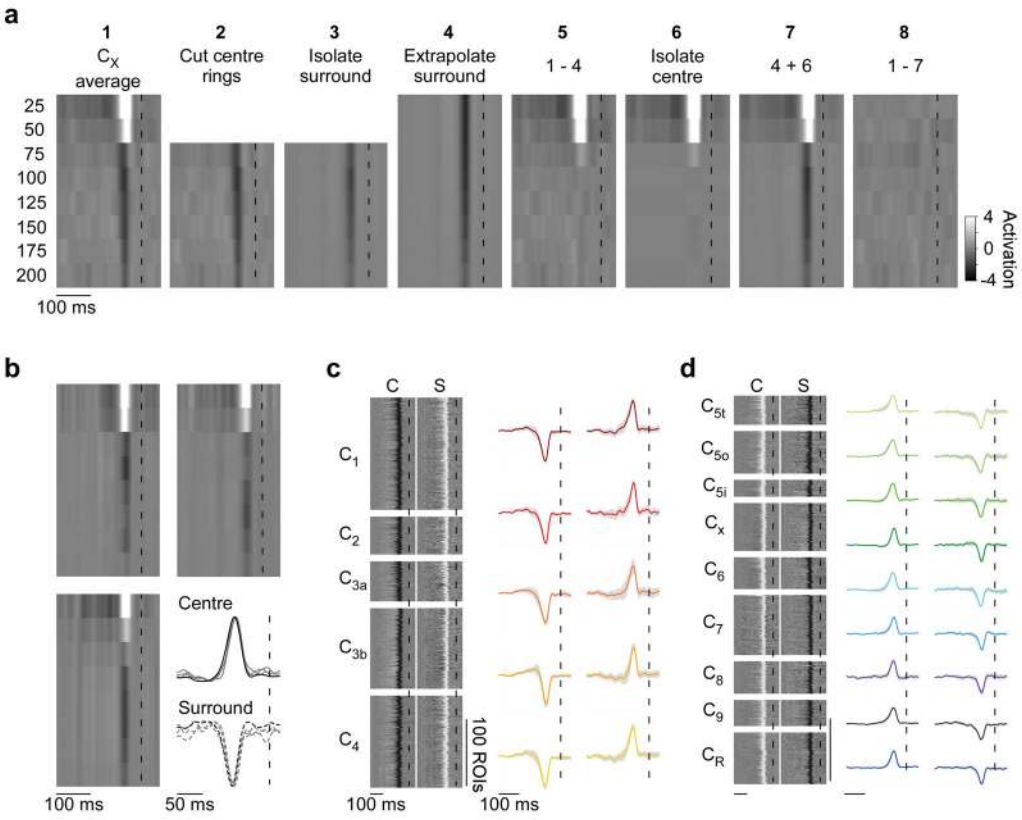

Extended Data Figure 9. Extraction of BC centre-surround RFs

a, Centre-surround maps obtained from the ring noise were averaged across ROIs assigned to one cluster (1). To isolate the surround component, the innermost two rings which contained the majority of the centre component were clipped (2) and the surround map estimated by SVD (3) was extrapolated across the centre by fitting a Gaussian (4). Next, the extrapolated surround map was subtracted from the average map and the centre component was extracted using SVD (6). The resultant centre-surround map was then subtracted from the average map to estimate the residual variance (7, Methods). Dotted lines at t=0. **b,** Centre-surround maps of 3 ROIs assigned to C_X from three independent experiments (*top;*

bottom, left). Overlaid centre and surround time kernels (*bottom, right*) of ROIs (*grey*) and cluster mean (*black*) illustrate temporal precision and reproducibility. **c**,**d,** Heat maps of all centre (C) and surround (S) time kernels and cluster means ± s.d. for Off (c) and On (d) BC clusters.

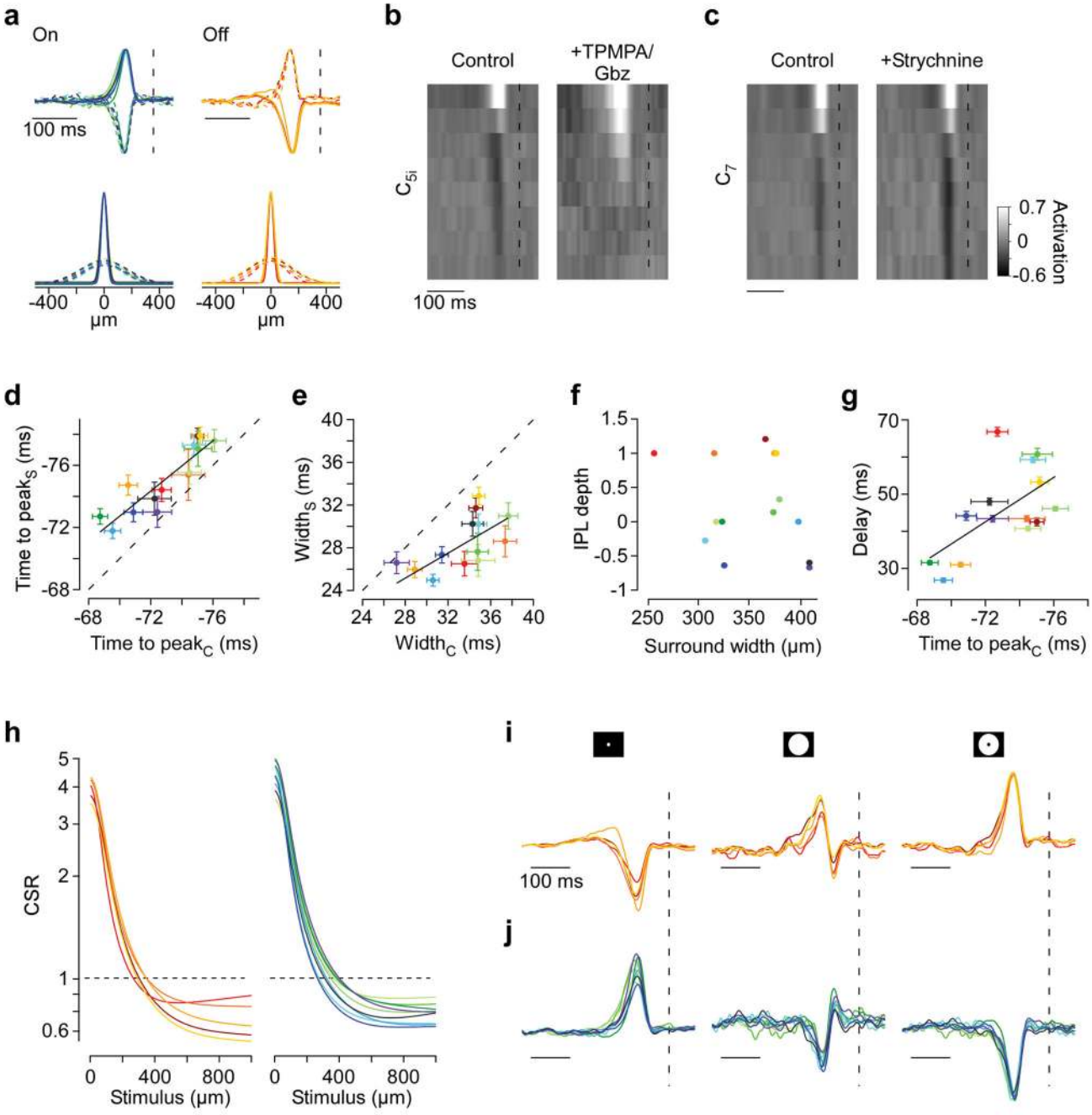

Extended Data Figure 10. Centre-surround RFs of BC clusters

a, Normalised time (*top*) and space (*bottom*) kernels of all On and Off BC clusters. Space kernels represent extrapolated Gauss fits of centre and surround activation across rings shown in (Fig. 5b), with circles corresponding to the original data points (Methods). **b,c,**

Effect of GABA (b) and glycine (c) receptor block on centre-surround RFs of two exemplary BC clusters. Centre-surround maps correspond to averages of n>5 ROIs of one scan field. **d,** Time to peak of centre time kernels preceded peak of surround time kernels (cluster mean ± s.e.m.; r=0.91, p<0.001, n=14, linear correlation), consistent with at least two additional synapses in the inhibitory pathway. Black line corresponds to linear fit and for the dashed line the slope=1. **e,** Half-maximal width (cluster mean± s.e.m.) was consistently narrower for centre compared to surround time-kernels (r=0.83, p<0.001, n=14, linear correlation). **f,** Half-maximal width of surround space kernels did not correlate with mean cluster IPL depth (r=0.06, p>0.05, n=14, linear correlation). **g,** Time to peak of centre time kernels correlated with response delay estimated from local chirp step responses (mean ± s.e.m.; r=0.82, p<0.001, n=14, linear correlation), indicating that centre kernels adequately reflect BC responses to local stimuli. **h,** Predicted centre-surround ratios (CSRs) of BC clusters for different stimulus diameters (cf. Fig. 5d). **i,j,** Normalised temporal kernels predicted for local (100 μm diameter), full-field (500 μm diameter) and surround-only (500 and 100 μm outer and inner diameter, respectively) stimulation for Off (i) and On (j) BC clusters (cf. Fig. 5e), respectively.

Supplementary Material

Refer to Web version on PubMed Central for supplementary material.

Acknowledgments

We thank G. Eske for technical support, C. Behrens for help with EM data, J. Jüttner (Roska lab, FMI for Biomedical Research, Basel) for help with virus injection and X. Pitkow and R. Taylor for discussion. We thank Loren L. Looger, the Janelia Research Campus of the Howard Hughes Medical Institute and the Genetically-Encoded Neuronal Indicator and Effector (GENIE) Project for making the viral constructs (AAV9.hSyn.iGluSnFR.WPRE.SV40, AAV9.CAG.Flex.iGluSnFR.WPRE.SV40 and AAV9.Syn.Flex.GCaMP6f.WPRE.SV40) publically available. This work was supported by the Deutsche Forschungsgemeinschaft (DFG; EXC307; BA 5283/1-1 to T.B.; BE 5601/1-1 to P.B.), the German Federal Ministry of Education and Research (BMBF; FKZ 01GQ1002 to M.B. and T.E.; FKZ 01GQ1601 to P.B.), the BW-Stiftung (AZ 1.16101.09), the intramural *f*ortüne program of the University of Tübingen (2125-0-0 to T.B.), the European Commission (H2020 ERC-StG 677687 "NeuroVisEco" to T.B.), the National Institute of Neurological Disorders and Stroke (U01NS090562 to T.E.) and National Eye Institute (1R01EY023766 to T.E.) of the National Institutes of Health. The content is solely the responsibility of the authors and does not necessarily represent the official views of the funders.

References

1. Masland RH. The Neuronal Organization of the Retina. Neuron. 2012; 76:266–280. [PubMed: 23083731]
2. Baden T, et al. The functional diversity of retinal ganglion cells in the mouse. Nature. 2016; 529:345–350. [PubMed: 26735013]
3. Sanes JR, Masland RH. The Types of Retinal Ganglion Cells: Current Status and Implications for Neuronal Classification. Annu Rev Neurosci. 2015; 38:221–46. [PubMed: 25897874]
4. Euler T, Haverkamp S, Schubert T, Baden T. Retinal bipolar cells: elementary building blocks of vision. Nat Rev Neurosci. 2014; 15:507–19. [PubMed: 25158357]
5. Helmstaedter M, et al. Connectomic reconstruction of the inner plexiform layer in the mouse retina. Nature. 2013; 500:168–74. [PubMed: 23925239]
6. Kim JS, et al. Space-time wiring specificity supports direction selectivity in the retina. Nature. 2014; 509:331–6. [PubMed: 24805243]

7. Behrens C, Schubert T, Haverkamp S, Euler T. Connectivity map of bipolar cells and photoreceptors in the mouse retina. Elife. 2016 in press.
8. Wässle H, Puller C, Muller F, Haverkamp S. Cone Contacts, Mosaics, and Territories of Bipolar Cells in the Mouse Retina. J Neurosci. 2009; 29:106–117. [PubMed: 19129389]
9. Shekhar K, et al. Comprehensive Classification of Retinal Bipolar Neurons by Single-Cell Transcriptomics Resource Comprehensive Classification of Retinal Bipolar Neurons by Single-Cell Transcriptomics. Cell. 2016; 166:1308–1323.e30. [PubMed: 27565351]
10. Greene MJ, Kim JS, Seung HS. Analogous Convergence of Sustained and Transient Inputs in Parallel On and Off Pathways for Retinal Motion Computation. Cell Rep. 2016; 14:1–9. [PubMed: 26725109]
11. Awatramani GB, Slaughter MM. Origin of transient and sustained responses in ganglion cells of the retina. J Neurosci. 2000; 20:7087–7095. [PubMed: 10995856]
12. Breuninger T, Puller C, Haverkamp S, Euler T. Chromatic Bipolar Cell Pathways in the Mouse Retina. J Neurosci. 2011; 31:6504–6517. [PubMed: 21525291]
13. Euler T, Schneider H, Wassle H. Glutamate responses of bipolar cells in a slice preparation of the rat retina. J Neurosci. 1996; 16:2934–2944. [PubMed: 8622124]
14. DeVries SH. Bipolar cells use kainate and AMPA receptors to filter visual information into separate channels. Neuron. 2000; 28:847–856. [PubMed: 11163271]
15. DeVries SH, Li W, Saszik S. Parallel Processing in Two Transmitter Microenvironments at the Cone Photoreceptor Synapse. Neuron. 2006; 50:735–748. [PubMed: 16731512]
16. Lindstrom SH, Ryan DG, Shi J, DeVries SH. Kainate receptor subunit diversity underlying response diversity in retinal Off bipolar cells. J Physiol. 2014; 592:1457–1477. [PubMed: 24396054]
17. Puller C, Ivanova E, Euler T, Haverkamp S, Schubert T. OFF bipolar cells express distinct types of dendritic glutamate receptors in the mouse retina. Neuroscience. 2013; 243:136–148. [PubMed: 23567811]
18. Puthussery T, et al. Kainate receptors mediate synaptic input to transient and sustained OFF visual pathways in primate retina. J Neurosci. 2014; 34:7611–21. [PubMed: 24872565]
19. Masland RH. The tasks of amacrine cells. Vis Neurosci. 2012; 29:3–9. [PubMed: 22416289]
20. Eggers ED, Lukasiewicz PD. Multiple pathways of inhibition shape bipolar cell responses in the retina. Vis Neurosci. 2011; 28:95–108. [PubMed: 20932357]
21. Grimes WN, Li W, Chávez AE, Diamond JS. BK channels modulate pre- and postsynaptic signaling at reciprocal synapses in retina. Nat Neurosci. 2009; 12:585–592. [PubMed: 19363492]
22. Demb JB, Singer JH. Intrinsic properties and functional circuitry of the AII amacrine cell. Vis Neurosci. 2012; 29:51–60. [PubMed: 22310372]
23. Marvin JS, et al. An optimized fluorescent probe for visualizing glutamate neurotransmission. Nat Methods. 2013; 10:162–170. [PubMed: 23314171]
24. Borghuis BG, Marvin JS, Looger LL, Demb JB. Two-photon imaging of nonlinear glutamate release dynamics at bipolar cell synapses in the mouse retina. J Neurosci. 2013; 33:10972–85. [PubMed: 23825403]
25. Chen M, Lee S, Park SJH, Looger LL, Zhou ZJ. Receptive field properties of bipolar cell axon terminals in direction-selective sublaminas of the mouse retina. J Neurophysiol. 2014; 112:1950–1962. [PubMed: 25031256]
26. Rosa JM, et al. Crossover Inhibition Generates Sustained Visual Responses in the Inner Retina. Neuron. 2016; 90:308–319. [PubMed: 27068790]
27. Dreosti E, Esposti F, Baden T, Lagnado L. In vivo evidence that retinal bipolar cells generate spikes modulated by light. Nat Neurosci. 2011; 14:951–952. [PubMed: 21706020]
28. Baden T, Berens P, Bethge M, Euler T. Spikes in Mammalian Bipolar Cells Support Temporal Layering of the Inner Retina. Curr Biol. 2013; 23:48–52. [PubMed: 23246403]
29. Burrone J, Lagnado L. Synaptic Depression and the Kinetics of Exocytosis in Retinal Bipolar Cells. J Neurosci. 2000; 20:568–578. [PubMed: 10632586]
30. Nikolaev A, Leung KM, Odermatt B, Lagnado L. Synaptic mechanisms of adaptation and sensitization in the retina. Nat Neurosci. 2013; 16:934–41. [PubMed: 23685718]

31. Chen TW, et al. Ultrasensitive fluorescent proteins for imaging neuronal activity. Nature. 2013; 499:295–300. [PubMed: 23868258]
32. Werblin FS, Dowling JE. Organization of the retina of the mudpuppy, Neturus maculosis. II Intracellular recording. J Neurophysiol. 1969; 32:339–355. [PubMed: 4306897]
33. Roska B, Werblin FS. Vertical interactions across ten parallel, stacked representations in the mammalian retina. Nature. 2001; 410:583–587. [PubMed: 11279496]
34. Lukasiewicz PD, Werblin FS. A novel GABA receptor modulates synaptic transmission from bipolar to ganglion and amacrine cells in the tiger salamander retina. J Neurosci. 1994; 14:1213–23. [PubMed: 7907138]
35. Euler T, Masland RH. Light-evoked responses of bipolar cells in a mammalian retina. J Neurophysiol. 2000; 83:1817–29. [PubMed: 10758094]
36. Euler T, Wässle H. Different contributions of GABAA and GABAC receptors to rod and cone bipolar cells in a rat retinal slice preparation. J Neurophysiol. 1998; 79:1384–1395. [PubMed: 9497419]
37. Vaney DI. The Mosaic of Amacrine Cells in the Mammalian Retina. Prog Retin Res. 1990; 9:49–100.
38. Eggers ED, Lukasiewicz PD, Eggers ED, Lukasiewicz PD. Interneuron Circuits Tune Inhibition in Retinal Bipolar Cells. 2010; 103:25–37.
39. Roska B, Nemeth E, Orzo L, Werblin FS. Three levels of lateral inhibition: A space-time study of the retina of the tiger salamander. J Neurosci. 2000; 20:1941–1951. [PubMed: 10684895]
40. Ichinose T, Lukasiewicz PD. Inner and outer retinal pathways both contribute to surround inhibition of salamander ganglion cells. J Physiol. 2005; 565:517–35. [PubMed: 15760938]
41. Buldyrev I, Taylor WR. Inhibitory mechanisms that generate centre and surround properties in ON and OFF brisk-sustained ganglion cells in the rabbit retina. J Physiol. 2013; 591:303–25. [PubMed: 23045347]
42. Liang Z, Freed MA. The ON Pathway Rectifies the OFF Pathway of the Mammalian Retina. J Neurosci. 2010; 30:5533–5543. [PubMed: 20410107]
43. Zaghloul KA, Boahen K, Demb JB. Different Circuits for ON and OFF Retinal Ganglion Cells Cause Different Contrast Sensitivities. 2003; 23:2645–2654.
44. Atick JJ, Redlich AN. Towards a theory of early visual processing. Neural Comput. 1990; 320:1–13.
45. Barlow H. Possible principles underlying the transformations of sensory messages. Sensory communication. 1961; 6:57–58.
46. Pitkow X, Meister M. Decorrelation and efficient coding by retinal ganglion cells. Nat Neurosci. 2012; 15:628–635. [PubMed: 22406548]
47. Vinje WE, Vinje WE, Gallant JL. Sparse Coding and Decorrelation in Primary Visual Cortex During Natural Vision. 2007; 1273:1273–1276.
48. Wiechert MT, Judkewitz B, Riecke H, Friedrich RW. Mechanisms of pattern decorrelation by recurrent neuronal circuits. Nat Neurosci. 2010; 13:1003–1010. [PubMed: 20581841]
49. Denève S, Machens CK. Efficient codes and balanced networks. Nat Neurosci. 2016; 19:375–382. [PubMed: 26906504]
50. Kemmler R, Schultz K, Dedek K, Euler T, Schubert T. Differential regulation of cone calcium signals by different horizontal cell feedback mechanisms in the mouse retina. J Neurosci. 2014; 34:11826–43. [PubMed: 25164677]
51. Schubert T, et al. Development of presynaptic inhibition onto retinal bipolar cell axon terminals is subclass-specific. J Neurophysiol. 2008; 100:304–316. [PubMed: 18436633]
52. Euler T, et al. Eyecup scope-optical recordings of light stimulus-evoked fluorescence signals in the retina. Pflugers Arch Eur J Physiol. 2009; 457:1393–1414. [PubMed: 19023590]
53. Baden T, et al. A tale of two retinal domains: Near-Optimal sampling of achromatic contrasts in natural scenes through asymmetric photoreceptor distribution. Neuron. 2013; 80:1206–1217. [PubMed: 24314730]
54. Yatsenko D, et al. DataJoint: managing big scientific data using MATLAB or Python. 2015; :1–10. DOI: 10.1101/031658

55. Dorostkar MM, Dreosti E, Odermatt B, Lagnado L. Computational processing of optical measurements of neuronal and synaptic activity in networks. J Neurosci Methods. 2010; 188:141–150. [PubMed: 20152860]

56. Baden T, et al. The functional diversity of retinal ganglion cells in the mouse. Nature. 2016; 529:345–350. [PubMed: 26735013]

57. Baden T, Berens P, Bethge M, Euler T. Spikes in Mammalian Bipolar Cells Support Temporal Layering of the Inner Retina. Curr Biol Biol. 2013; 23:48–52.

58. Greene MJ, Kim JS, Seung HS. Analogous Convergence of Sustained and Transient Inputs in Parallel On and Off Pathways for Retinal Motion Computation. Cell Rep. 2016; 14:1–9. [PubMed: 26725109]

59. Kim JS, et al. Space-time wiring specificity supports direction selectivity in the retina. Nature. 2014; 509:331–6. [PubMed: 24805243]

60. Szczurek E, Biecek P, Tiuryn J, Vingron M. Introducing knowledge into differential expression analysis. J Comput Biol. 2010; 17:953–67. [PubMed: 20726790]

61. Bishop, CM. Pattern Recognition and Machine Learning. Springer; 2006.

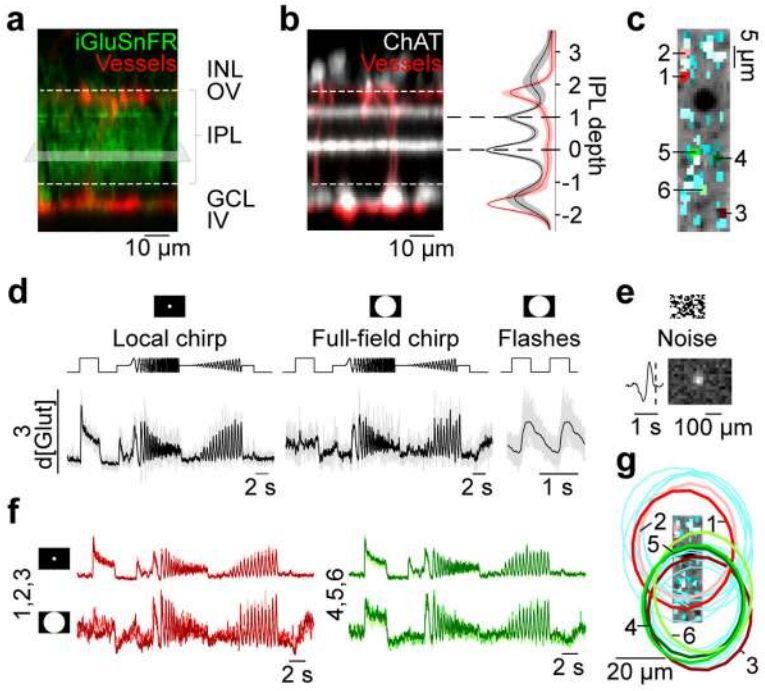

Figure 1. Imaging light-driven glutamate release in the IPL

a, Vertical projection of stack showing iGluSnFR expression (*green*) across the IPL, blood vessels in *red*. Grey plane: scan field orientation. GCL: Ganglion cell layer, IPL: Inner plexiform layer, INL: Inner nuclear layer, OV: Outer vessels, IV: Inner vessels. **b,** ChAT bands (*white*) relative to blood vessels (*red*) and average depth profiles (± s.d. shading); n=9 stacks, n=3 mice. **c,** Example scan field (64×16 pixels) with region-of-interest (ROI) mask. **d,** Glutamate response of ROI from (c) to local and full-field chirp stimulus and full-field flashes. *Black*: mean; *grey*: individual trials. Glutamate traces represent relative glutamate release (d[Glut]). **e,** Temporal and spatial receptive field of ROI from (d). Dashed line: Time of response. **f,** Superimposed mean glutamate traces in response to local (*top*) and full-field chirp (*bottom*) of red and green ROIs from (c). **g,** Scan field and ROI mask from (c) with spatial RFs (2 s.d. outlines, n=20 ROIs) of red and green ROIs.

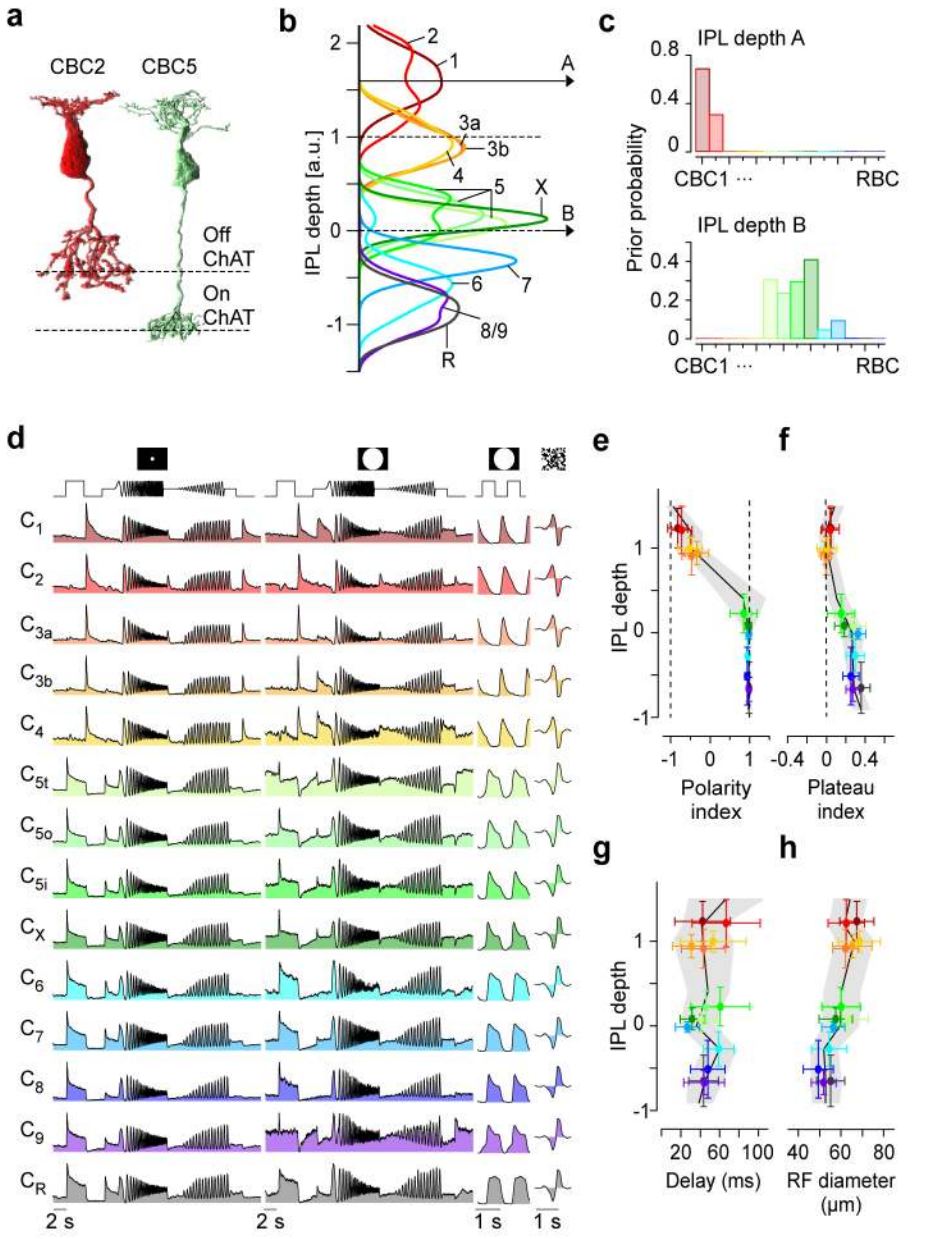

Figure 2. Anatomy-guided clustering and functional organisation of the IPL

a, EM-reconstructed example BCs from[5]. **b,** Mean BC stratification profiles of all known BCs (see text). Colours indicate cluster allocation in all subsequent figures. **c,** Prior probabilities of scan fields recorded at two IPL depths (A: 1.7; B: 0). **d,** Mean glutamate response (n=8,448 ROIs) of every cluster to local and full-field chirp, full-field flashes and temporal RF kernels. **e,** Polarity index (Methods) (n=8,448) as function of IPL depth. Shading corresponds to median ± s.d. for every IPL bin (n=13 bins). Cluster means (± s.d.) are overlaid. **f–h** like e for plateau index, delay and receptive field diameter (Methods). e–g were estimated from local chirp step responses.

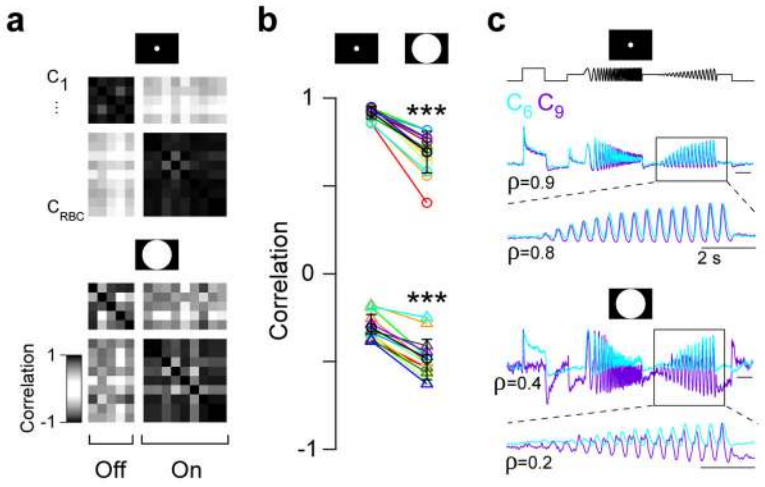

Figure 3. Surround activation increases functional diversity across BCs

a, Correlation between cluster means of local (*top*) and full-field (*bottom*) chirp responses. **b,** Mean correlation between local and full-field chirp responses for each cluster with all other clusters of the same (*top*) and opposite (*bottom*) polarity (mean: ρ_{local} =0.9 vs. $\rho_{full\text{-}field}$=0.7 and ρ_{local} =−0.3 vs. $\rho_{full\text{-}field}$=−0.5, p<0.001, n=14, non-parametric paired Wilcoxon signed-rank test). Mean ± s.d. in black. **c,** Mean chirp responses of C_6 and C_9, with linear correlation coefficient (ρ) of whole trace or contrast ramp.

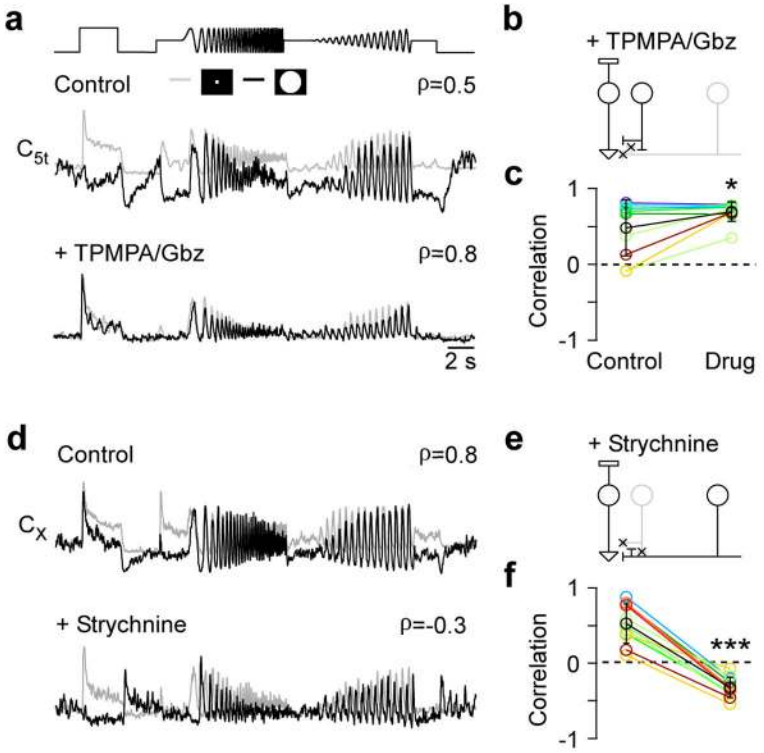

Figure 4. Opposite effects of GABA- and glycinergic ACs on BC output

a, Local (*grey*) and full-field (*black*) chirp responses for control condition and GABA receptor block, with linear correlation coefficient (ρ) between each pair. **b,** Schematic illustrating the effects of GABA receptor block (TPMPA/Gbz; 75/10 μM). **c,** Linear correlation coefficients of local and full-field chirp responses across different clusters for GABA receptor block ($p<0.05$, n=10 from 5 scan fields and 4 mice, non-parametric paired Wilcoxon signed-rank test). **d–f** like a–c but for glycine receptor block (Strychnine; 0.5 μM). $p<0.001$, n=8 from 4 scan fields and 3 mice.

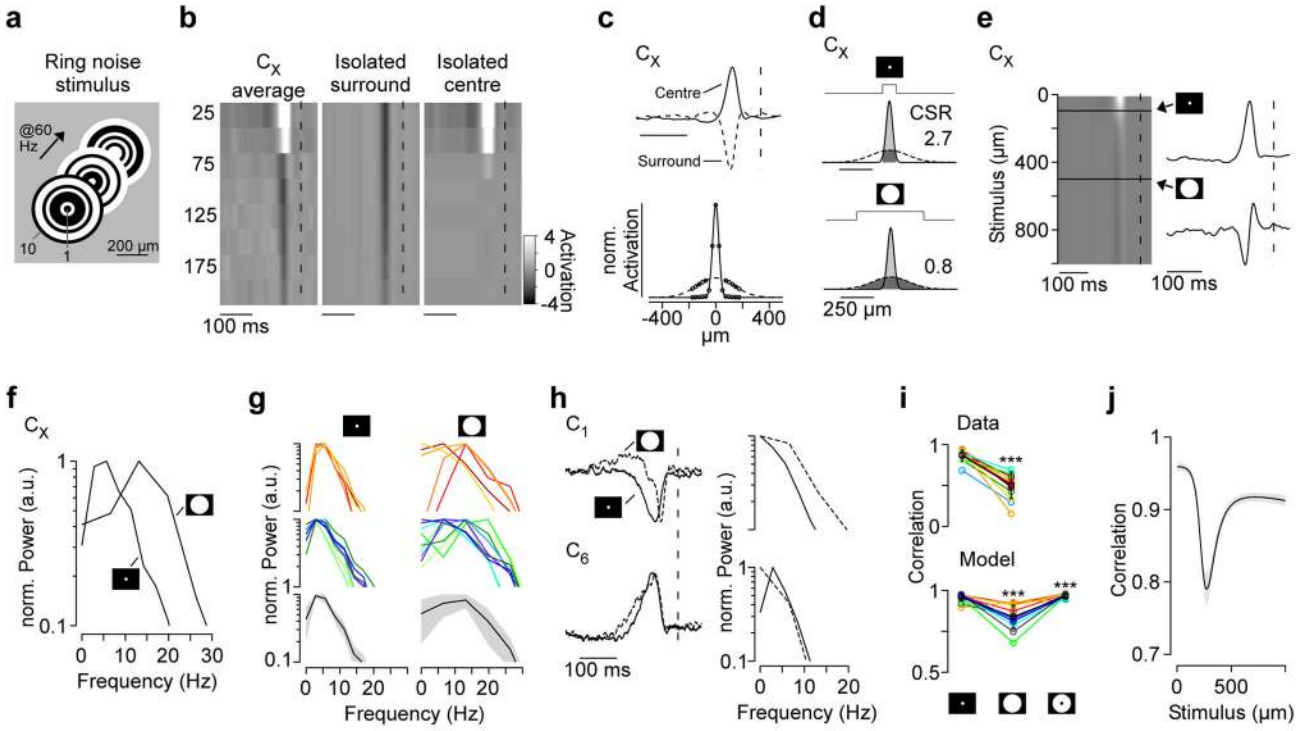

Figure 5. Differential centre-surround organisation underlies BC functional diversity

a, Schematic of ring noise stimulus (ring width: 25 µm). **b,** Centre-surround time kernels of an example cluster for 8 rings (C_X; Methods, cf. Extended Data Fig. 9a). Dashed line at t=0. **c,** Normalised time (*top*) and space (*bottom*) kernels of C_X. Space kernels are Gaussian fits of centre and surround activation, circles indicate original data points (Methods). **d,** Predicted centre-surround activation ratios (CSRs) to local (*top*) and full-field (*bottom*) spot-stimuli from activation of centre (*light grey*) and surround (*dark grey*). **e,** Normalised effective time kernels of C_X for different stimulus diameters (*left*) and for 100 and 500 µm (*right*). **f,** Normalised spectra of predicted time kernels shown in (e, *right*). **g,** Normalised spectra predicted for Off- (*top*) and On-clusters (*middle*) during local (*left*) and full-field (*right*) stimulation with mean ± s.d. shown in black/grey (*bottom*). **h,** Measured time kernels (*left*) and frequency spectra (*right*) for a local and full-field spot noise stimulus (C_1 and C_6). **i,** Measured and predicted correlation of time kernels for local, full-field and surround-only stimulation (data: $p<0.001$, n=13, non-parametric paired Wilcoxon signed-rank test; model: both $p<0.001$, n=14). Black: mean ± s.d.. **j,** Average correlation ± s.e.m. across predicted cluster time kernels for different stimulus diameters.